

AD-A271 009



FINAL REPORT

DAMPING IN FERROUS SHAPE MEMORY ALLOYS

CONTRACT NUMBER: N00014-90-C-0076

DTIC
ELECTE
OCT 15 1993
S A D

By

L. McD. Schetky
M.H. Wu
C.Y. Lei
MEMRY TECHNOLOGIES, INC.
Brookfield, Connecticut

And

C.M. Wayman
Department of Materials Science and Engineering
University of Illinois

And

M. Wuttig
Materials Engineering
University of Maryland

This document has been approved
for public release and sale; its
distribution is unlimited.

August 1993

93-23605



03-10 6-156

ABSTRACT

The damping properties of Fe-Mn-Si, Fe-Ni-Co-Ti and Fe-Al-C alloy systems were examined by DMTA and oscillation methods. The martensite transformations and microstructures were studied and examined by TEM, resistivity, and DSC. High damping was found in FeMnSi and FeNiCoTi alloys with microstructures containing glissile inter-variant martensite interfaces, while those with sessile inter-variant martensite interfaces exhibit lower damping. The general agreement between the damping peaks and transformation temperatures further confirms the close relations between high damping and shape memory behavior.

Accession For	
NTIS (R&D)	<input checked="" type="checkbox"/>
DTIC (R&D)	<input type="checkbox"/>
Unannounced	<input type="checkbox"/>
Justification	
By A 233543	
Distribution	
Availability Codes	
Dist	Avail. & Status
A-1	

DTIC QUALITY INSPECTED 2

TABLE OF CONTENTS

I. INTRODUCTION	1
1. High Damping Alloys	1
1-a. Mn-Cu Alloys	2
1-b. Ferromagnetic Alloys	2
1-c. Shape Memory Alloys	3
2. Shape Memory Effect	3
2-a. One-way Memory Effect	3
2-b. Two-way Memory Effect	5
2-c. Pseudoelasticity	7
3. Ferrous Shape Memory Alloys	7
3-a. ϵ (hcp) martensite	10
3-b. γ' (fct) martensite	10
3-c. α' (bct) martensite	10
4. Damping in Ferrous Shape Memory Alloys	11
5. Program Objective	11
II. EXPERIMENTAL	12
1. Selection of Alloy Compositions	12
1-a. Fe-Mn-Si-X	12
1-b. Fe-Ni-Ti-Co	12
1-c. Fe-Al-C	12
2. Specimen Preparation and Materials Characterizations	12
3. Damping Measurements	13
III. RESULTS	15
1. Fe-Mn-Si Based Alloys	15
1-a. Transformation Temperatures and Neel temperatures	15
1-b. Shape Memory Effect	20
1-c. Mechanical Properties	20
1-d. Martensite Morphology and Shape Memory Mechanism	25
2. Fe-Ni-Ti-Co Alloys	30
2-a. Transformation Temperatures	30
2-b. Shape Memory Effect	30
2-c. Microstructures and Martensite Morphology	35
3. Fe-Al-C System	35
3-a. Transformation Temperatures	35
3-b. Microstructures and Martensite Morphology	43
3-c. Mechanical and Shape Memory Properties	43
4. Damping Properties	43
4-a. Fe-Mn-Si-Ni-Cr Alloy	43
4-b. Fe-Ni-Ti-Co Alloy	53
IV. DISCUSSION	56
1. Shape Memory Effect of Ferrous SMA	56
2. Damping in Ferrous SMA	57
V. CONCLUSIONS	59
REFERENCES	60

I. INTRODUCTION

Modern naval surface and underwater crafts require careful design of all machine systems which can be the source of noise and vibration. Naval warfare relies on the strategic use of submarines, not only as a means for control of the seas by interdiction of commercial and military ships, but also as a platform for launching missiles. Both the hunter and the hunted must preserve their security by stealth, which means that silence is a paramount part of the strategy.

Noise which can be detected by an adversary can be from many sources: the hydrodynamic noise of the hull and propellers, noise from drive shaft bearings and reduction gearing, vibration from stationary auxiliary diesel generators as well as from the main power plant, noise from fluid control valves and associated pumps, and noise from general crew activities.

Noise and vibration control may be approached by isolation, dissipation or both. The isolation approach prevents energy transmission from the noise sources to the radiation surfaces. For examples, noise can be reduced by enclosures, by isolation mounts or suspension systems or by improved tolerances of mating machine parts. Energy absorbing materials, such as polymeric materials, have been used widely for noise and vibration dissipation, either as a coating or as the inner of a constrained layer system, literally a sandwich of metallic and polymeric layers. However, all of these incur a penalty of weight, space or cost. For Naval submarines where space is limited and where sound is radiated through the hull into the sea, these approaches are not only difficult but also costly as well. For some time it has been proposed that the solution lies in the approach of energy dissipation by using metallic structural materials which have inherent high damping.

1. High Damping Alloys

The ability of a material to absorb vibration energy is usually designated by the specific damping capacity (SDC), defined as the percent energy dissipation in a single oscillation cycle:

$$SDC = \frac{A_n^2 - A_{n+1}^2}{A_n^2} \times 100\%$$

where A_n and A_{n+1} are the amplitudes of successive cycles of vibration. Conventional metals, such as steels, brasses, bronzes, aluminum alloys and essentially all high-strength alloys do not have high damping capacity. Their SDCs are in general less than 1%. Gray cast iron, which has the highest energy absorbing power among common structural materials, has an SDC in the range of 5-10%. The

internal damping mechanism in gray cast iron is related to the large, flake-like graphite particles which are effective in energy absorption.

High damping alloys are metals with damping capacity higher than that of gray cast iron. Energy dissipation in these alloys are related to lattice friction against the motion of microstructural interfaces^[1]. Damping of this type is typically strain-amplitude dependent and frequency independent. Due to different thermal stability of these microstructures, interface damping exhibits temperature dependence. Depending on the microstructure giving rise to high damping capacity, these high damping alloys fall into the following three categories:

1-a. Mn-Cu Alloys

Alloys containing more than 30 wt.% Mn are known to exhibit high damping after solution heat treatment and subsequent aging at 300-600°C of the f.c.c. γ phase. Aging induces continuous decomposition and creates Mn-rich regions where the f.c.c. phase transforms into f.c.t. structure. The f.c.t. phase is antiferromagnetic, ordered and appears in twin-related domains separated by the {100} atomic boundaries. The energy dissipation mechanism was suggested to be related to the hysteresis loss associated with the movement of these boundaries^[2], as the vibration causes the rotation of the f.c.t. antiferromagnetic domains. Mn-Cu alloys have good strength and a reasonable modulus, but suffer with respect to fabricability.

Several commercial applications have been evaluated and show promises. Sonoston, developed by British Stone Manganese Marine Ltd., has been evaluated for ship propellers applications by some European navies with reported good performance. Incramute, another Mn-Cu based high damping alloy developed by International Copper Research Association, although showing potential in a number of industries: mining equipment, textile machinery, components in natural gas distribution systems, and automotive manufacturing plants, has never achieved commercial production.

1-b. Ferromagnetic alloys, such as Fe-Cr alloys

High damping Fe-Cr alloys contain 12-16 wt.%Cr. These alloys go through a ferromagnetic transition on cooling through the Curie temperature at approximately 700°C. High damping was attributed to a large magnetomechanical hysteresis loss associated with the magnetostrictive movement of magnetic domain walls driven by outside excitation^[3]. Damping of Fe-Cr alloys exhibits strong dependence on magnetic field. Because of the high Curie temperature, these alloys have potential for higher temperature applications than Mn-Cu alloys and shape memory alloys. Although Fe-Cr based alloys exhibit high damping at lower strain level than Mn-Cu alloys, the damping saturates at relatively low stress levels.

Commercial ferromagnetic high damping alloys include Fe-Cr based alloys such as Silentalloy (Toshiba Co.), Tranqualloy (Nippon Steel Co.), and Vacrosil (Vacuumschmelzer GMBH), as well as Nivco (Westinghouse), a Co-Ni based alloy. Fe-Cr based alloys have been used as standard materials for turbine blades. Ferromagnetic high damping alloys also have possible applications in automobiles and electrical machinery.

1-c. Shape memory alloys (SMA), such as Ni-Ti, Cu-Al-Ni, and Cu-Zn-Al

Shape memory alloys undergo a thermoelastic martensitic transformation which yields multiple martensite variants along equivalent crystallographic orientations. The frictional loss associated with the motion of the intervariant interfaces gives rise to high damping when excited by applied cyclic stress. Thermoelastic martensites can also be induced by stress at temperatures above the transformation temperature. The interfaces between martensite and the parent matrix is also mobile and reversible. The hysteresis effect of these interfaces exhibits even higher damping than that of the intervariant interfaces. The mechanism, however, operates in a much narrower temperature range. The critical excitation stress for high damping in shape memory alloys is higher than that in Mn-Cu or Fe-Cr alloys. Shape memory alloys in their martensitic condition, which is necessary for high damping, exhibit low modulus which make these alloys unsuitable for structural components.

Among various shape memory alloys, Cu-Zn-Al alloys have been evaluated for use as a structural damper to reduce structural damage from earthquakes^[3]. The results, although less effective than viscoelastic dampers, were satisfactory. The study suggested that SMA may be better suited for base isolation. NiTi alloys have been used as actuators for active vibration control in smart material systems with proven success^[4].

The damping characteristics of several selected metals are listed in a comparative Table I together with their yield strength and density^[1,5].

2. Shape Memory Effect (SME)

2-a. One-way memory effect

Thermoelastic martensitic transformations in shape memory alloys occur in a narrow temperature range with a small temperature hysteresis. The transformation temperatures and hysteresis are defined in Figure 1. Thermoelastic martensitic transformation yields martensite variants of alternately sheared platelet. These platelets appear in groups such that the shear deformation of each platelets in the group is accommodated with each other. No overall deformation is present in association with the transformation. Transforming from a single β crystal (Figure 2(a)), the self

Table I. Damping Characteristics of Selected Metals at Room Temperature^[1].

Metal	SDC(%)	Yield Strength (10³ psi)	Density (g/cm³)
Wrought Mg alloys	49	26	1.74
Cu-Mn alloys	40	45	7.5
Ni-Ti alloys	40	25	6.45
Fe-Cr-Al alloys	40	40	7.4
Cu-Al-Ni-Mn alloys ^[5]	40	19	7.1
Cu-Zn-Al alloys ^[5]	30	12	7.64
High C gray iron	19	25	7.7
Pure Ni	18	9	8.9
Pure Fe	16	10	8.9
Martensitic stainless steel	8	85	7.7
Gray cast iron	6	25	7.8
SAP Al powder	5	20	2.55
Low C steel	4	50	7.86
Ferritic stainless steel	3	45	7.75
Malleable nodular cast irons	2	50	7.8
Medium C steel	1	60	7.86
Austenitic stainless steel	1	35	7.8
1100 Al	0.3	5	2.71
Al alloy (2024-T4)	<0.2	47	2.77
Ni base superalloys	<0.2	range	8.5
Ti alloys	<0.2	range	4.5
Brasses, bronzes	<0.2	range	8.5

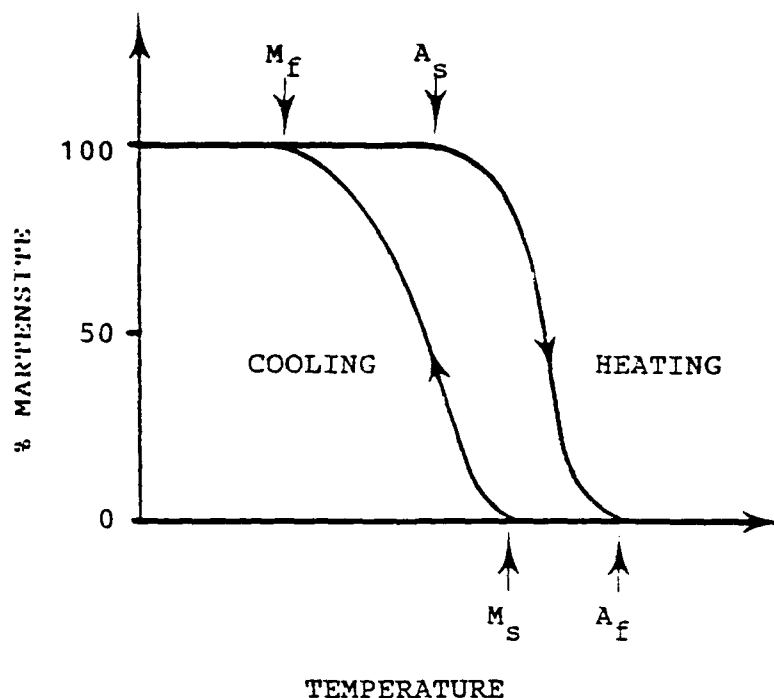
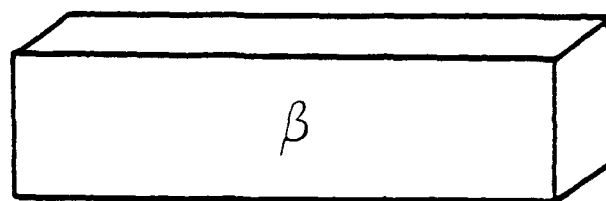


Figure 1. Transformation curve of thermoelastic martensite.

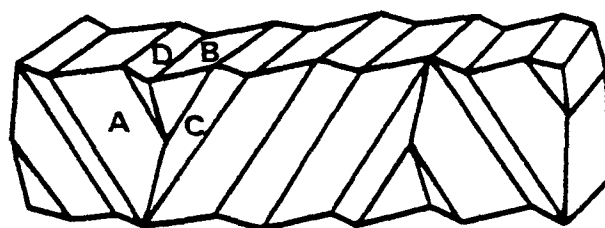
accommodation configuration is illustrated in Figure 2(b) with variants designated by A, B, C and D. When the self-accommodating martensite is deformed, a particular variant with orientation mostly favorably aligned with respect to the applied stress grows at the expense of other variants, eventually dominates the configuration, leading to a macroscopic strain, ϵ , as illustrated in Figure 2(c). Preferred orientation of martensite can also be created by stress-induced transformation at temperatures above the M_s temperature. The mechanical behavior associated with this deformation process is shown in the stress-strain curve in Figure 3. At $T < M_f$, the reorientation of martensite variants starts at σ_c and the deformation is retained upon release of stress. On heating, the martensite transforms back to the parent β phase (Figure 2(a)) and the strain is recovered following a strain-temperature curve passing through A_s and A_f temperatures in Figure 3. This shape recovery is termed "One-Way Memory Effect".

2-b. Two-way memory effect

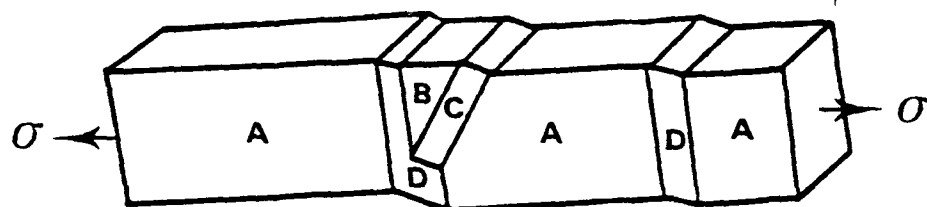
Two-way memory effect allows a specimen to assume one shape when in the martensitic phase and another shape when in the parent phase state, and spontaneously change from one shape to the other



(a) $T > A_f$



(b) $T < M_f$



(c) $T < M_f$

Figure 2. (a) Single crystal β phase, (b) self-accommodation of martensite and (c) martensitic structure with preferred variant under stress.

on heating and cooling. Two-way memory effect can be achieved by a thermomechanical processing called "training" which involves stabilizing the preferred martensite variants on cooling. This is achieved by constraining the preferred martensite variant during shape recovery on heating. The process induces microstress in the parent phase, which promotes the formation of preferred martensite variants and creates a macroscopic strain during cooling. When the specimen is again heated the normal memory process takes place and the original shape is recovered. The thermomechanical behavior of two-way memory effect is described by a close loop going through M_s , M_f , A_s and A_f temperature on the strain-temperature plane in Figure 3.

2-c. Pseudoelasticity

At temperatures above the A_f temperature, the stress-induced martensite is not stable and will transform back to the parent β phase upon the removal of stress. Shape recovery thus occurs instantaneously during unloading. Pseudoelasticity is described in a stress-strain loop at temperatures between A_f and M_d temperatures in Figure 3. The yield stress, σ_c , corresponding to the critical stress required to induced martensite, increases linearly with temperature. The M_d temperature is defined as the temperature at which σ_c equals to the yield stress of conventional dislocation slip. Above the M_d temperature, the specimen deforms by slip at stress lower than σ_c while the stress-induced martensitic transformation becomes infeasible.

Most common shape memory alloys include Ni-Ti, Cu-Zn-Al and Cu-Al-Ni Alloys. The physical properties, mechanical properties and their transformation properties are listed in Table II.

3. Ferrous Shape Memory Alloys

In ferrous alloys, an f.c.c. γ austenite can transform to three different types of martensite depending on the alloy systems.

- (1) ϵ martensite (hcp) in Fe-Mn and Fe-Cr-Ni alloys.
- (2) γ' martensite (fct) in Fe-Pd and Fe-Pt alloys.
- (3) α' martensite (bct) in Fe-Ni and Fe-C alloys

Both ϵ and γ' martensites adopt thin plate morphology. In case of α' martensite, four distinct morphologies have been observed; lath, butterfly, lenticular and thin plate. Lath martensites occur at high temperatures while butterfly and lenticular morphologies dominate the intermediate temperature range. Thin plate martensites transform only at low temperatures. The four types of martensites are distinguished in their crystallography as well. Lath martensite exhibit primarily dislocation fine structure. Both butterfly and lenticular martensites are partially twinned while thin plate martensite is fully twinned.

The formation of these morphologies are dictated by the

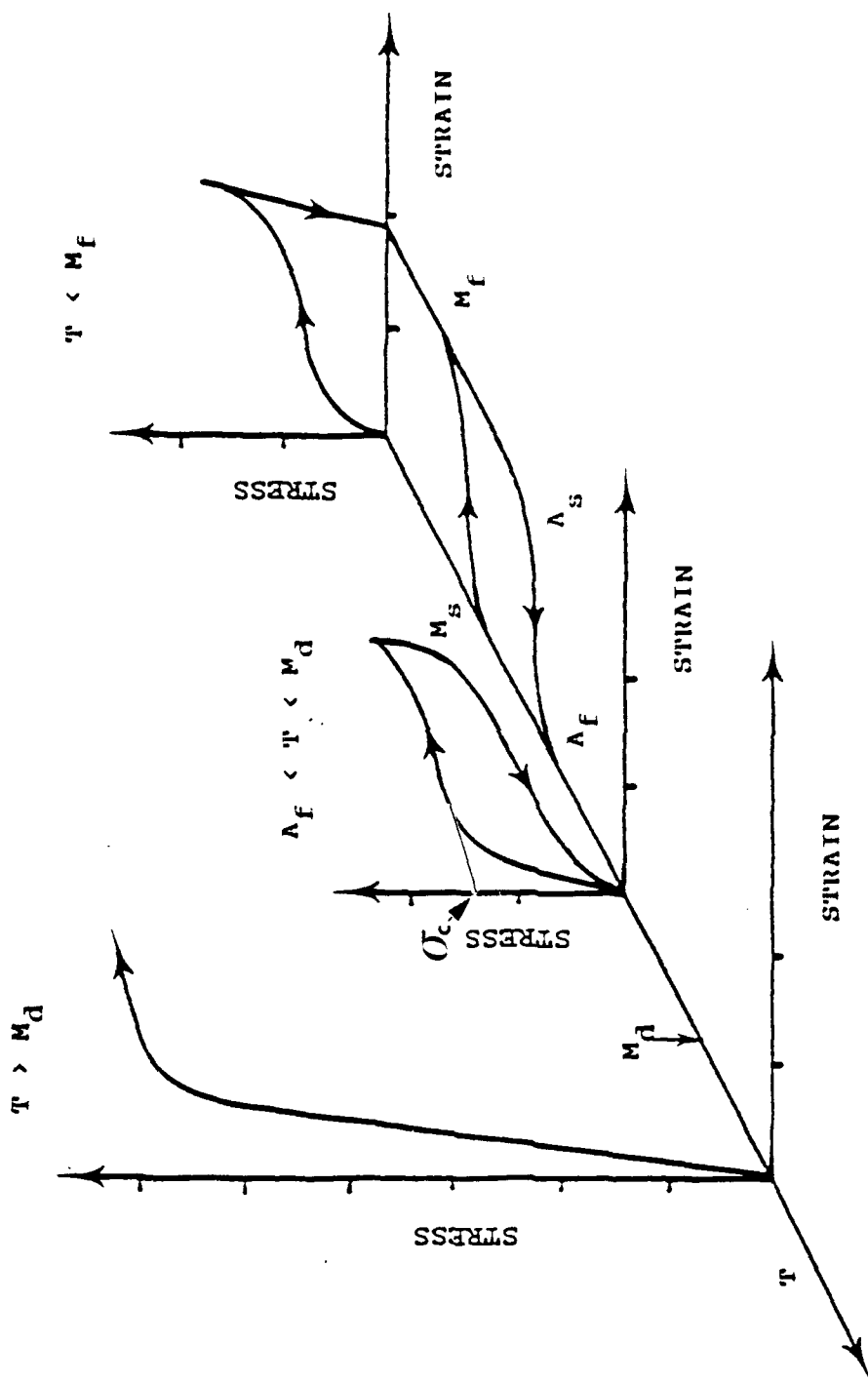


Figure 3. Stress-strain-temperature characteristics of shape memory alloy.

Table II. PROPERTIES OF SHAPE MEMORY ALLOYS

PHYSICAL PROPERTIES	Cu-Zn-Al	Cu-Al-Ni	Ni-Ti
Density (g.m ³)	7.64	7.12	6.5
Resistivity ($\mu\Omega\cdot\text{cm}$)	8.5-9.7	11-13	80-100
Thermal Conductivity (J/m ² ·s·K)	120	30-43	10
Heat Capacity (J/Kg·K)	400	373-574	390

MECHANICAL PROPERTIES	Cu-Zn	Cu-Al-Ni	Ni-Ti
Young's Modulus (GPa)			
β -Phase	72	35	83
Martensite	70	30	34
Yield Strength (MPa)			
β -Phase	350	400	690
Martensite	80	130	70-150
Ultimate Tensile Strength (MPa)	600	500-800	900

TRANSFORMATION PROPERTIES	Cu-Zn-Al	Cu-Al-Ni	Ni-Ti
Heat of Transformation (J/mole)			
Martensite	160-440	310-470	295
R-Phase			55
Hysteresis (K)			
Martensite	10-25	15-20	30-40
R-Phase			2-5
Recoverable Strain (%)			
One-Way (Martensite)	4	4	8
One-Way (R-Phase)			0.5-1
Two-Way (Martensite)	2	2	3

transformation driving force. Lath, butterfly and lenticular martensites transform at a large driving force and follow a burst-type of kinetics. Because of a severe plastic relaxation of transformation strain, the interfaces of these morphologies are not mobile. Thin plate martensites, on the other hand, transform with a small driving force. The transformation follows steady growth kinetics. The interface is mobile as less plastic relaxation occurs in the vicinity of transformation. It was suggested that the absence of plastic accommodation of the transformation strain allows the martensite interfaces to preserve their mobility and reversibility which are essentially the necessary conditions for shape memory effect. Indeed, all ferrous martensites showing some degree of shape memory effect possess thin plate morphology.

3-a. ϵ (hcp) martensite

Enami et al.^[6] first discovered that 304 stainless steel (19%Cr, 10% Ni) shows an incomplete shape memory effect. Sato et al.^[7] and Murakami et al.^[8] have shown that Fe-Mn-Si alloys exhibit complete shape memory effect. Shape memory effect in Fe-Mn-Si alloys can be improved by adding C to strengthen the austenite matrix^[9]. More recently, both NKK^[10] and Nippon Steel Corp.^[11] have developed Fe-Mn-Si based shape memory alloys by adding Cr and Ni to improve corrosion resistance. Although Fe-Mn-Si alloys can exhibit complete shape memory effect from stress-induced ϵ martensite, the $\gamma \rightarrow \epsilon$ transformation is not considered thermoelastic as the hysteresis is fairly wide (80-100°C).

3-b. γ' (fct) martensite

The martensitic transformation in Fe-Pd alloys proceeds through two stages, γ (fcc) $\rightarrow \gamma'$ (fct) $\rightarrow \alpha'$ (bct). The $\gamma \rightarrow \gamma'$ is thermoelastic and gives rise to shape memory effect^[12]. Thermoelastic $\gamma \rightarrow \gamma'$ martensitic transformation and shape memory effect were also observed in ordered Fe-Pt alloys^[13].

3-c. α' (bct) martensite

Umemoto and Wayman^[14], in their study of Fe₃Pt alloys, observed that accompanying an increase in parent phase order, the γ (fcc) $\rightarrow \alpha'$ (bct) martensitic transformation kinetics change from nonthermoelastic to thermoelastic. Along with this transition, the martensite morphology changes from lenticular to thin plate. Both the M_s temperature and transformation hysteresis also decrease with increase in long range order. The authors suggested that a combination effect of a lower M_s temperature, smaller transformation volume change and twinning shear due to an increase in tetragonality in ordered martensite promotes thermoelasticity. Maki et al.^[15], on the other hand, observed that Fe-Ni-Ti-Co alloys exhibit thermoelastic martensitic transformation and complete shape memory effect when properly aged. It was shown that precipitation of coherent ordered γ' Ni₃Ti occurs during aging, which strengthens

the parent austenite and increases the tetragonality of the martensite. Thin plate α' martensite is observed in other Fe-Ni alloys, such as Fe-Ni-C^[16-18], Fe-Ni-Al^[19] and Fe-Al-C^[20]. All these alloys exhibit fairly strong austenite and high martensite tetragonality. Partial shape memory effect has been observed in Fe-Ni-C^[21], Fe-Ni-Al-C and Fe-Ni-Al-Co-C^[22] alloys.

Judging from the transformation characteristics of thin plate martensite, the following four conditions were proposed to be the favorable conditions for the formation of thin plate morphology and shape memory effect^[23].

- (1) high strength austenite
- (2) a small transformation volume change and shape change
- (3) low transformation temperatures
- (4) a high tetragonality of martensite

4. Damping in Ferrous Shape Memory Alloys

Sato et al.^[24] investigated the internal friction associated with the ϵ martensite in a Fe-Mn-Si-Cr alloy. The height of the internal friction peak was directly proportional to the amount of ϵ martensite present in the sample. The mechanism was suggested to be related to the frictional effect of the austenite/martensite interfaces. Damping properties of other ferrous shape memory alloys have not been studied in details.

5. Program Objective

The objective of this program is to understand the damping mechanism in association with thin plate martensitic transformations in ferrous shape memory alloys. The knowledge will provide guidelines for alloy development of high damping, high modulus ferrous shape memory alloys that can be used for noise and vibration control in U.S. Navy systems.

II. EXPERIMENTAL

1. Selection of Alloy Compositions

Alloy systems exhibiting ϵ martensite and α' martensite are included in the present study. Alloys exhibiting ϵ martensite are primarily modifications of Fe-Mn-Si system while alloys exhibiting α' martensite include Fe-Ni-Ti-Co and Fe-Al-C. Fe-Pd and Fe-Pt alloys exhibiting γ' martensite are excluded because of the high cost of Pt and Pd, and therefore less likely to be economical engineering materials.

1-a. Fe-Mn-Si-X

A total of nine compositions of modified Fe-Mn-Si alloys have been investigated in the present study. The compositions are listed in Table III. The selection of alloying elements is based on the following guidelines.

- i. To strengthen the austenite by solution hardening (Si, Al, Cr and Ni) and precipitation hardening (Nb and C).
- ii. To promote the glissile nature of martensite interfaces by reducing the stacking fault energy (Si, Mn and Co).
- iii. Sato et al.^[25] have shown that the antiferromagnetic transition suppresses the transformation of ϵ martensite. Co is added to adjust the Néel temperature.

1-b. Fe-Ni-Ti-Co

The composition of Fe-33wt.%Ni-12wt.%Co-5wt.%Ti was selected for the study of α' martensite and the effect of precipitation hardening induced thermoelasticity.

1-c. Fe-Al-C

Based on the work by Watanabe and Wayman^[20], Fe-7wt.%Al-2wt.%C alloys exhibit thin plate, fully twinned martensite of high tetragonality ($c/a = 1.14$). The alloy was selected to study the effect of martensite tetragonality.

2. Specimen Preparation and Materials Characterizations

Alloys of selected compositions were prepared by vacuum arc melting. After hot rolling, specimens were cut, solution treated and water quenched. Except for Fe-Mn-Si-Nb-C alloys, all Fe-Mn-Si based alloys were solution heat treated at 1023°C for 30-60 minutes. Fe-Mn-Si-Nb-C, Fe-Ni-Ti-Co and Fe-Al-C alloys were all solution treated at 1200°C for 60 minutes. Postquench aging for Fe-Mn-Si-Nb-C and Fe-Ni-Ti-Co alloys were carried out at 700-800°C as

necessary.

Electrical resistivity (ER), dilatometry and differential scanning calorimetry (DSC) were used for the determination of transformation temperatures using a slope-intercept technique; examples are illustrated in Figure 4. The Néel temperature was determined by magnetic susceptibility measurement. Both optical metallography and transmission electron microscopy (TEM) were used for the study of microstructure.

Shape recovery and other mechanical properties were studied by a combination of tensile testing and bend test. The bend test uses rectangular specimens of thickness, t , which were bent around a mandrel of diameter d , as illustrated in Figure 5. The bending strain is defined by $\epsilon = t/d$. The percentage of elastic recovery and memory recovery are calculated according to the following equations.

$$f_e = \theta_e / \pi, \quad f_{sme} = \theta_m / (\pi - \theta_e)$$

3. Damping Measurements

Damping tests were carried out using a Dynamic Mechanical Thermal Analyzer (DMTA) at David Taylor Naval Research Laboratory (DTNRL), under the supervision of Ms. Cathy Wong, and at the University of Maryland using a resonance technique, under the direction of Professor M. Wuttig. The test apparatus at the University of Maryland is schematically shown in Figure 6. The excitation of the reed through the force exerted by a constant gradient magnetic field on the permanent Sm-Co magnet assures a constant excitation at finite amplitude.

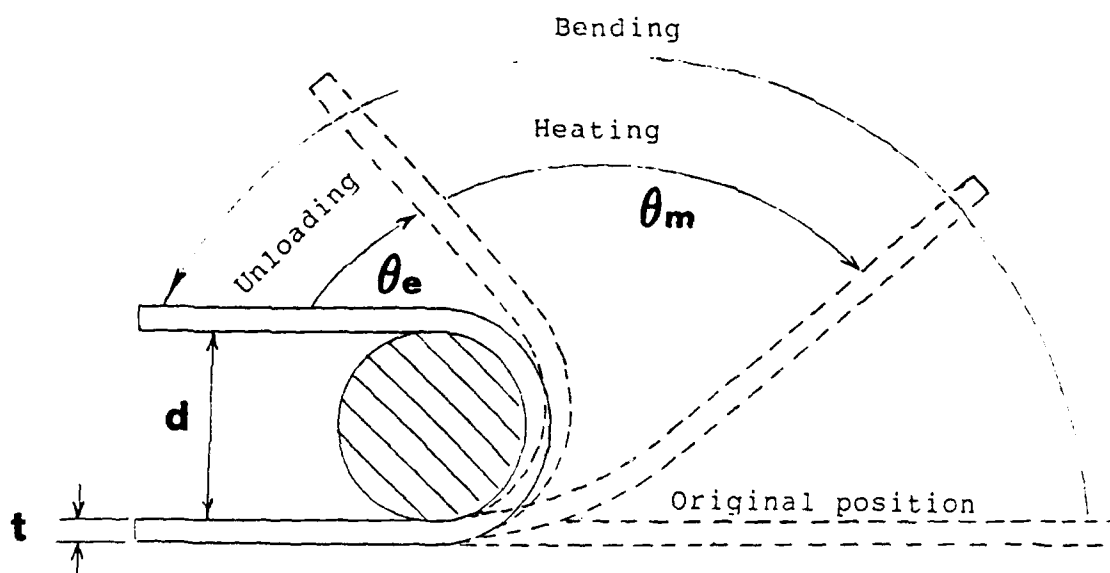


Figure 5. Bend test of shape memory effect.

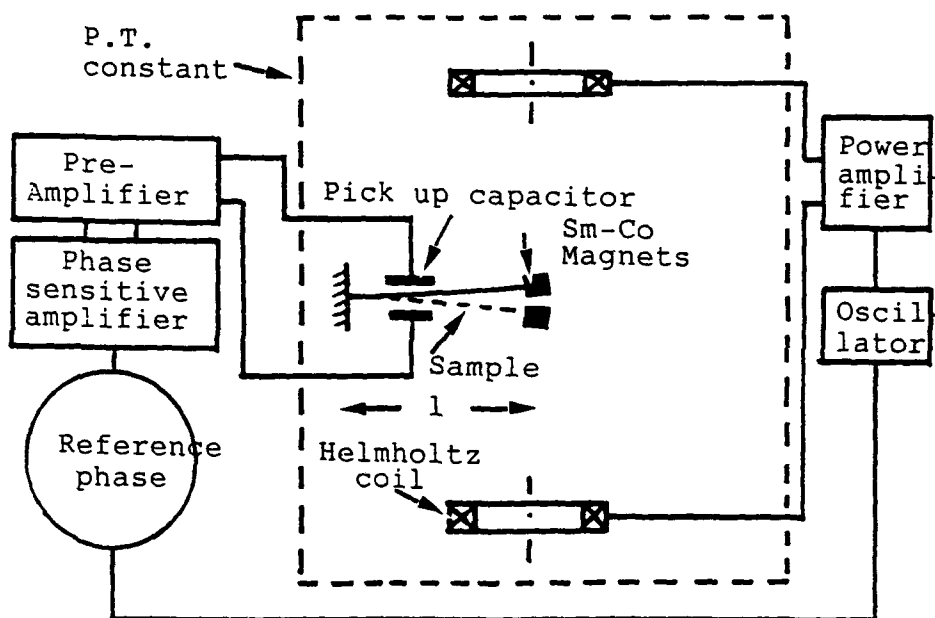


Figure 6. Schematic diagram of the resonance damping test instrumentation at the University of Maryland.

III. RESULTS

1. Fe-Mn-Si Based Alloys

Among the nine compositions listed in Table III, alloys # 2 and 3 were selected for further study because of their better shape memory effect. The two alloys also have very different Néel temperatures which makes them ideal for the study of the effect of antiferromagnetic transition. Alloy #9 is selected for the study the effect of precipitation strengthening.

Table III. Compositions (wt.%) of modified Fe-Mn-Si alloys.

Alloy #	Fe	Mn	Si	Cr	Ni	Co	Al	Nb	C
1	Bal.	30.0	7.0	5.0	2.5				
2	Bal.	13.8	6.0	8.4	5.0				
3	Bal.	29.0	5.5	4.5	2.0	3.5			
4	Bal.	30.0	5.0			4.0			
5	Bal.	30.0	6.0				2.0		
6	Bal.	31.0	2.0				4.0		
7	Bal.	27.0	6.0				5.0		
8	Bal.	25.0	4.0				2.0		
9	Bal.	32.0	6.0					0.05	0.04

1-a. Transformation Temperatures and Néel Temperatures

The resistivity and magnetic susceptibility curves of the three alloys are shown in Figures 7 and 8, respectively. Based on the amount of resistivity change, the amount of athermal martensitic transformation is more complete for alloy #2 than for the other two alloys after cooling to -196°C . The resistivity curves of alloys #3 and #9 also exhibit deflection in the temperature range of -50 to 0°C which is consistent with the Néel temperatures determined from the maxima of the magnetic susceptibility curves in Figure 8. It is evident that antiferromagnetic transition suppresses the martensitic transformation. A DSC curve and a dilatometry curve taken from alloy #2 after solution treatment are shown in Figures 9 and 10, respectively. Transformation temperatures and Néel temperatures determined from these curves are listed in Table IV. While the three techniques yield fairly close A_s and A_f temperatures, the M_s and M_f temperatures exhibit variation depending on the technique.

The transformations of alloy #2 exhibits aging effect. During aging of alloy #2 at $200-300^{\circ}\text{C}$, the transformation temperatures decrease while the transformation enthalpy increases as shown in Figures 11 and 12.

The resistivity curves of alloy #9 after NbC precipitation hardening treatments at 700 and 800°C for 5 hours are shown in

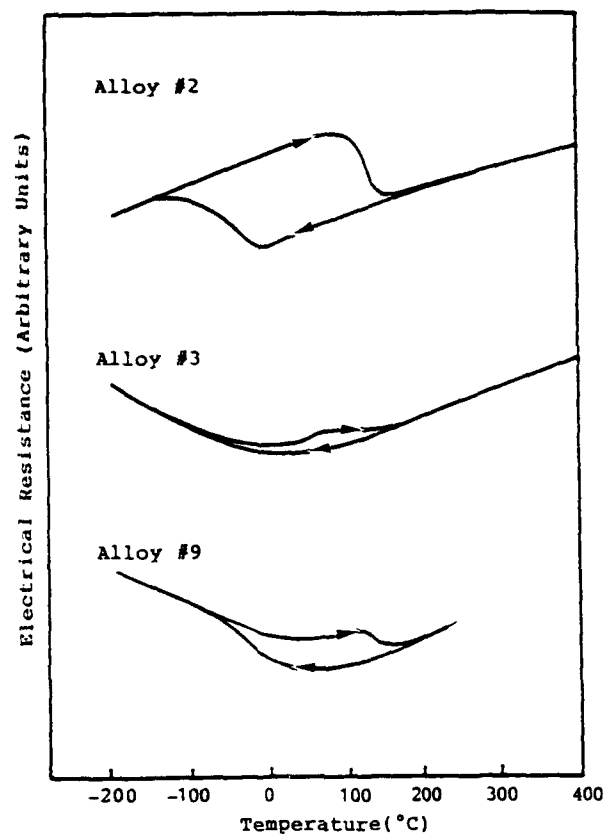


Figure 7. Change of electricity of alloys #2, 3, and 9 with temperature

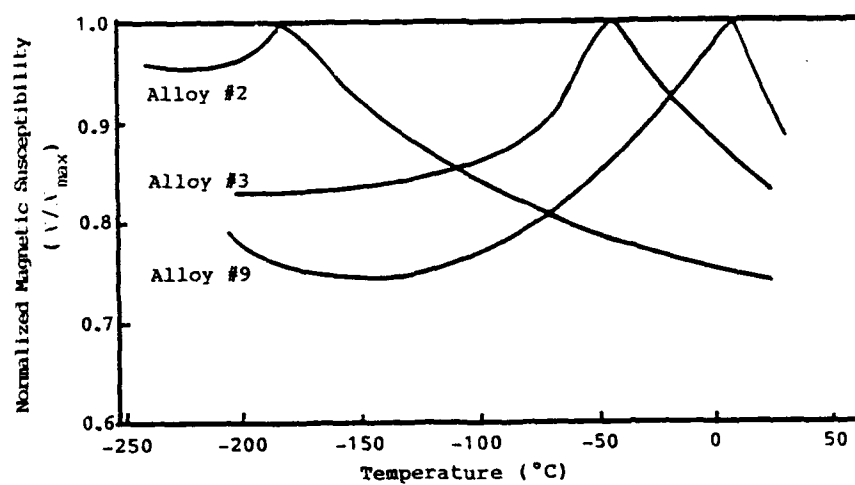


Figure 8. Change of Magnetic Susceptibility with temperature for alloys #2, 3 and 9.

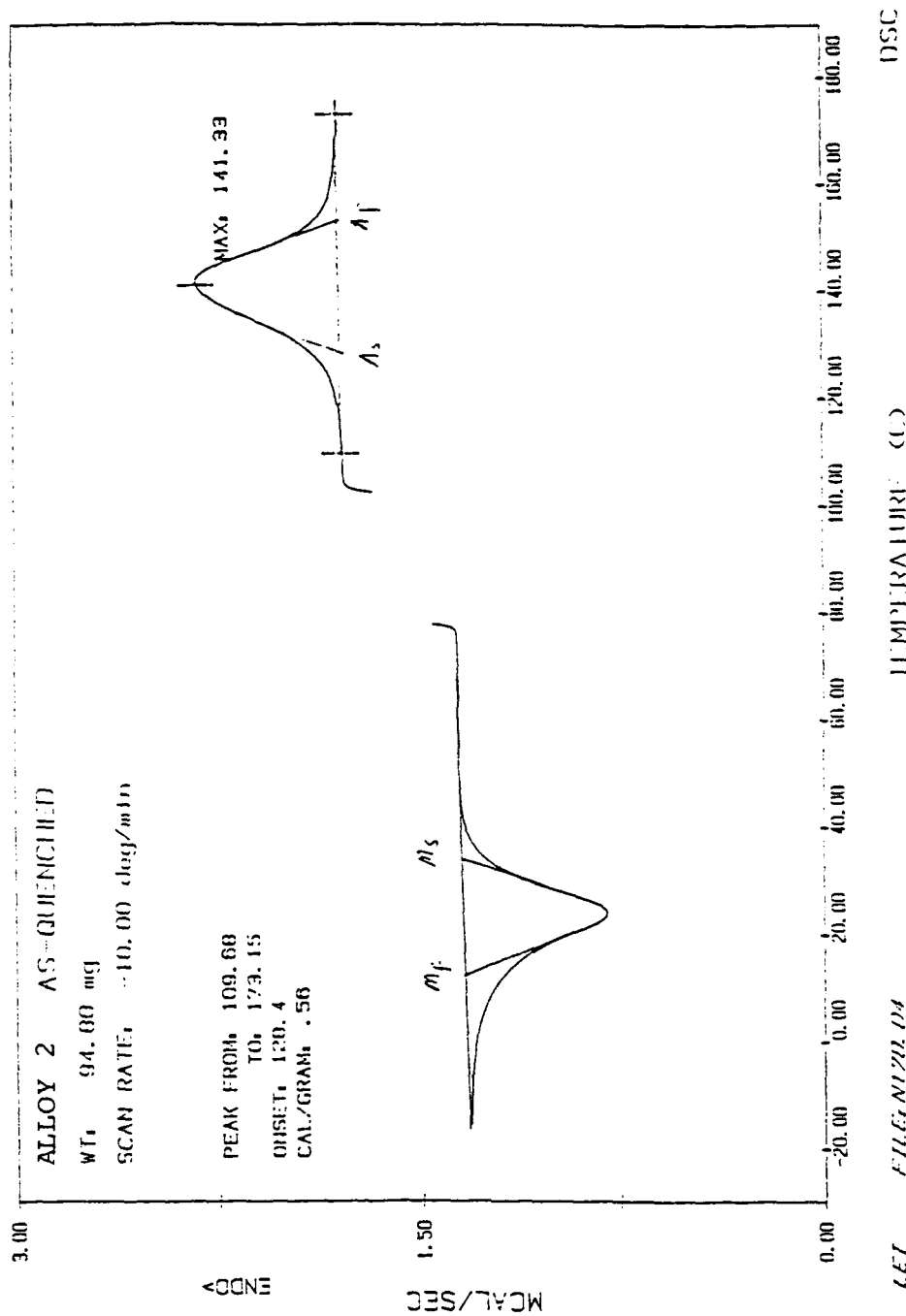


Figure 9. DSC curves of as-solution treated specimen.

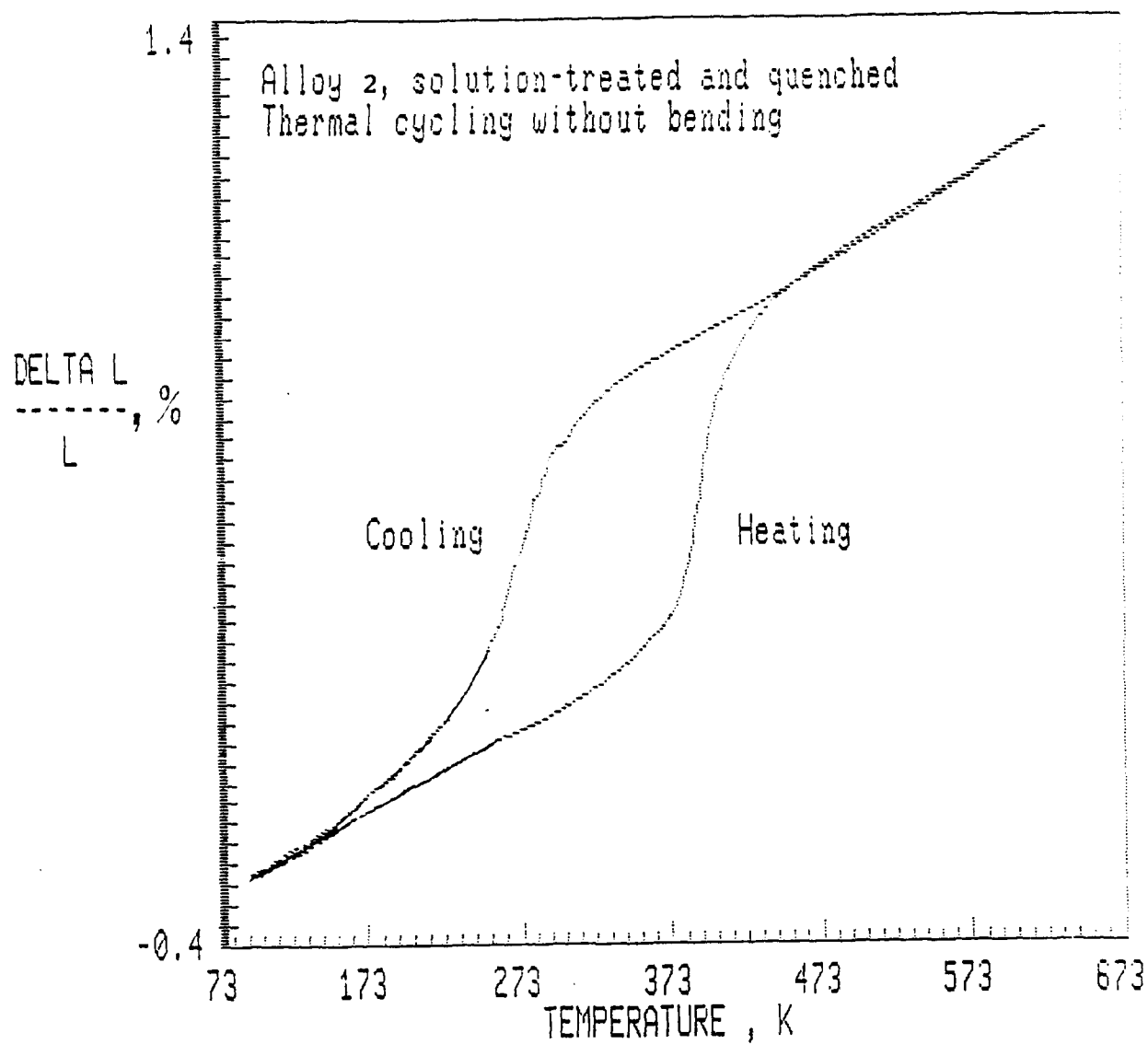


Figure 10. Dilatometry curve of alloy #2, showing the transformation hysteresis.

FeMSCN Transformation Temperatures

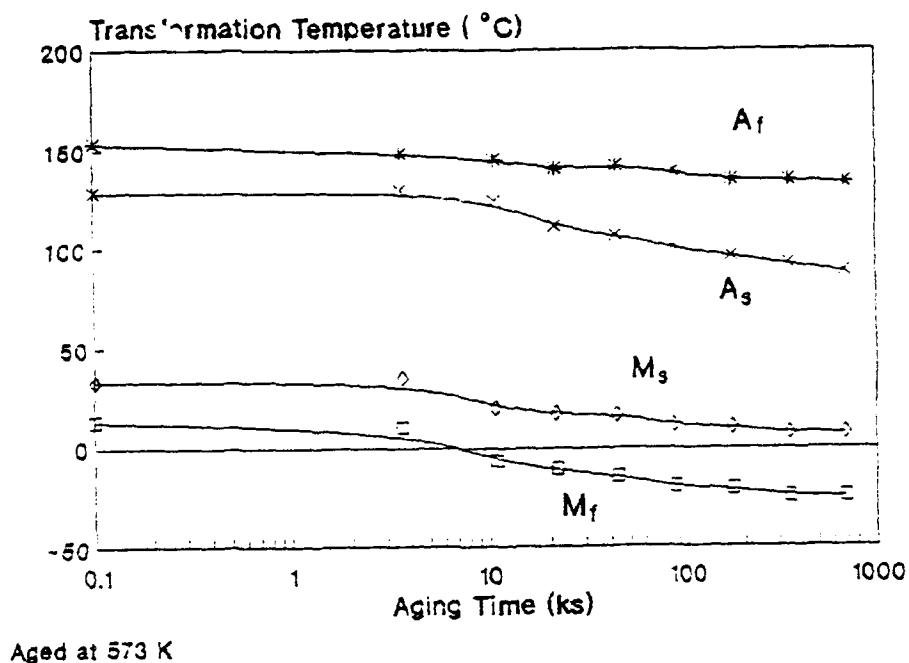


Figure 11. Effect of Aging on the Transformation Temperatures of Alloy #2

FeMSCN Transformation Heat

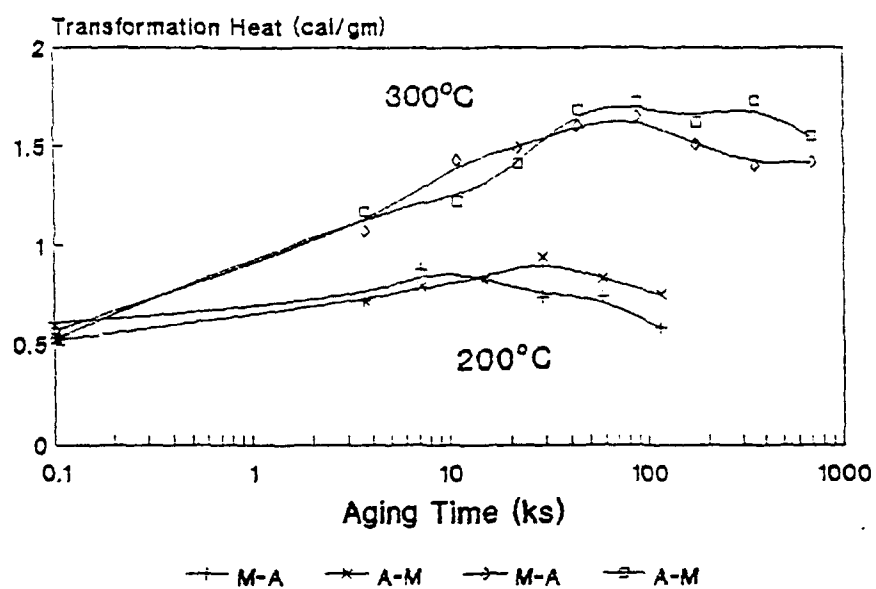


Figure 12. Effect of aging on the transformation heat of Alloy #2.

Figure 13. In comparison to those after solution heat treatment, both A_s and M_s temperatures increase after these aging treatments.

Table IV. Transformation temperatures determined by resistivity, dilatometry as well as DSC(*) measurements, and Néel temperatures (T_N) of modified Fe-Mn-Si alloys in °C.

Technique	Alloy #	A_s	A_f	M_s	M_f	T_N
Resistivity	2	114	147	-4	-94	-183
Dilatometry	2	106	143	36	-44	
DSC	2	128	153	34	12	
Resistivity	3	88	161	0	--	-43
Resistivity	9	118	154	43	--	8

1-b. Shape Memory Effect

Pseudoelastic strain (PE), shape memory strain (SME) and residual plastic strain (RS) of alloys #2 and #3, were determined by bend tests. The results are plotted in Figure 14 and 15, respectively. The effect of deformation temperature is also studied. According to Figure 14, deformation at ambient (300 K) or -196°C (77 K) yields the same shape recovery for alloy #2. For alloy #3, however, deformation at 77 K yields a much higher shape memory recovery than bending at ambient temperature (Figure 15). Maximum shape memory recovery strain is 5% and 4% for alloys #2 and #3, respectively.

The shape memory strain recovery of alloy #3 after various amounts of cold roll reduction of 5-35% and subsequent annealing at 650K (377°C) for 6 hours is plotted in Figure 16. Small amounts of cold work (5-15%) improve the shape memory strain recovery.

The shape memory recovery of alloy #9 in the as-quenched state and after postquench aging at 700 and 800°C was studied by tensile tests using an MTS tensile machine. The percentage of shape memory recovery is plotted against the deformation strain in Figures 17a, b and c. The data points along the curve were measured with deformation at room temperature and subsequently heating up to 400°C . Data points of comparison include those with deformation at -196°C , and those after thermomechanical cycling consisting of repetition of deformation at room temperature and subsequent heating to 400°C for 30 minutes. The amount of deformation is defined in the caption of the figure. Similar to alloy #3, both deformation at -196°C and thermomechanical cycling of alloy #9 improve the shape memory recovery. 700- 800°C aging improves only the shape recovery with lower than 2% initial deformation.

1-c. Mechanical Properties

A tensile specimen of alloy #2 after solution treatment was first cooled to -196°C and then tested at 50°C . The stress-strain

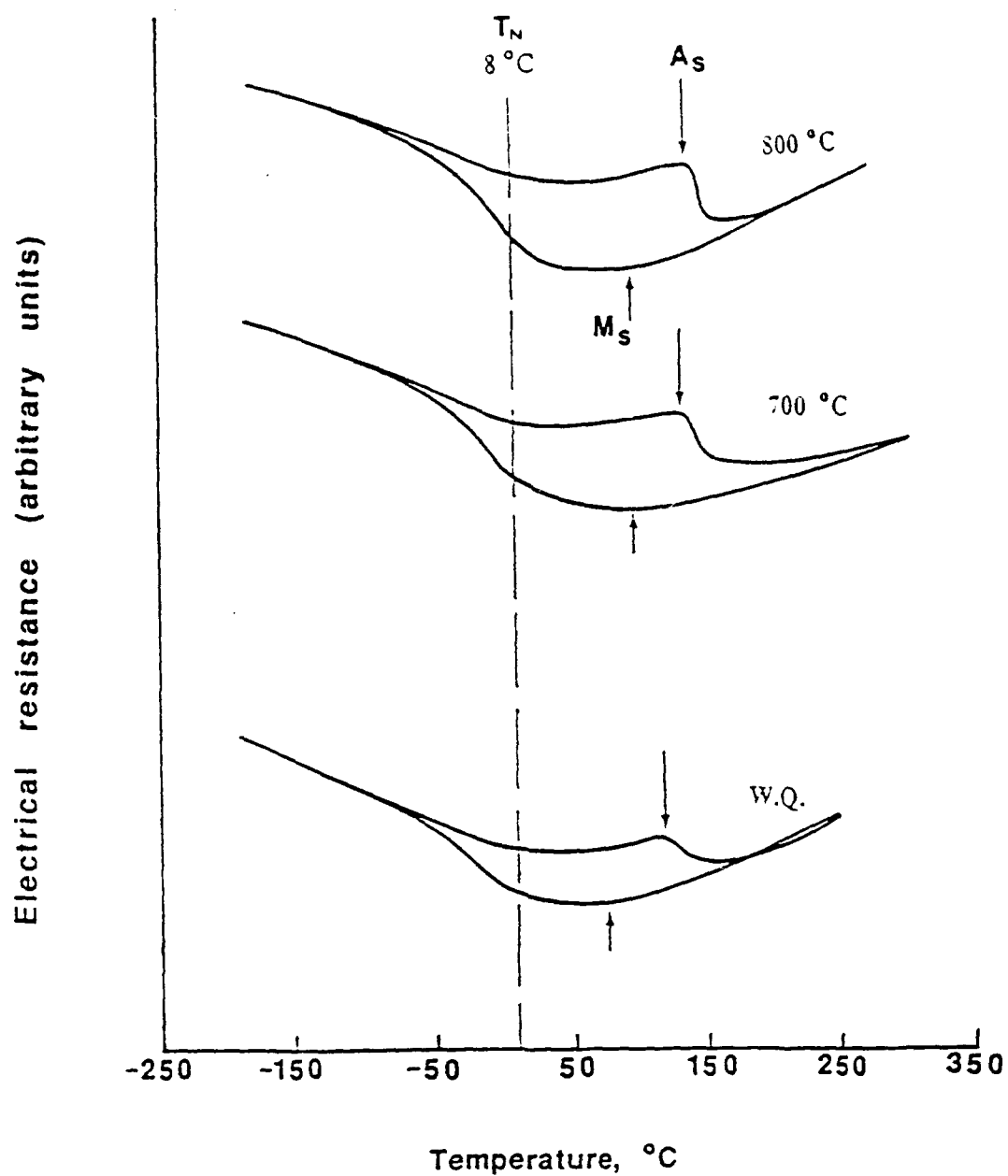


Figure 13. Resistivity change of alloy #9 with temperature after different heat treatments.

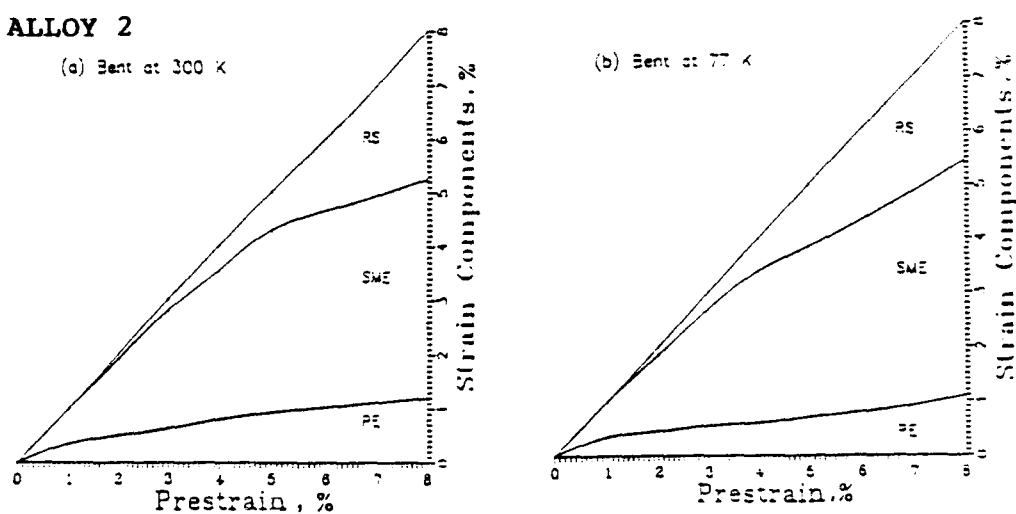
ALLOY 2

Figure 14. Bending test results showing the change of three strain components with total prestrain.

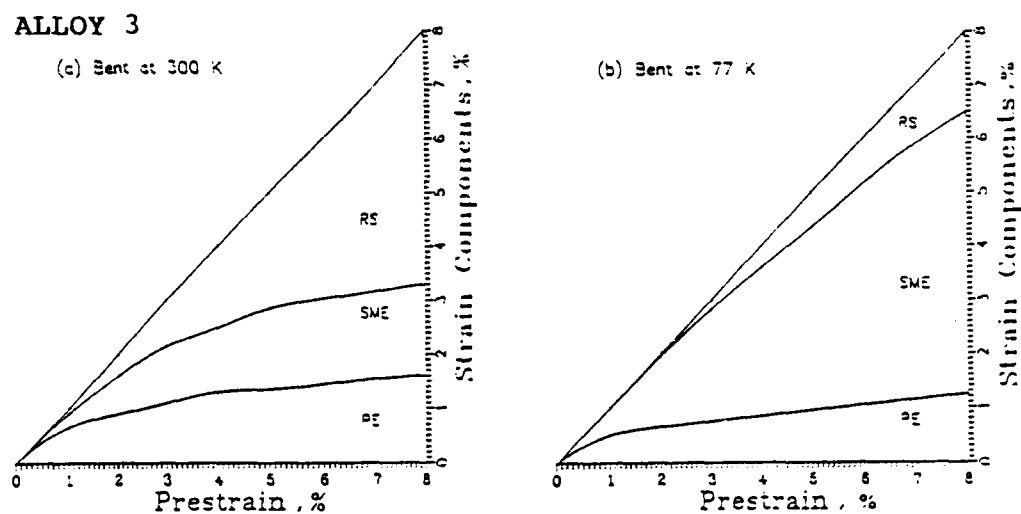
ALLOY 3

Figure 15. Bending test results showing the change of three strain components with total prestrain.

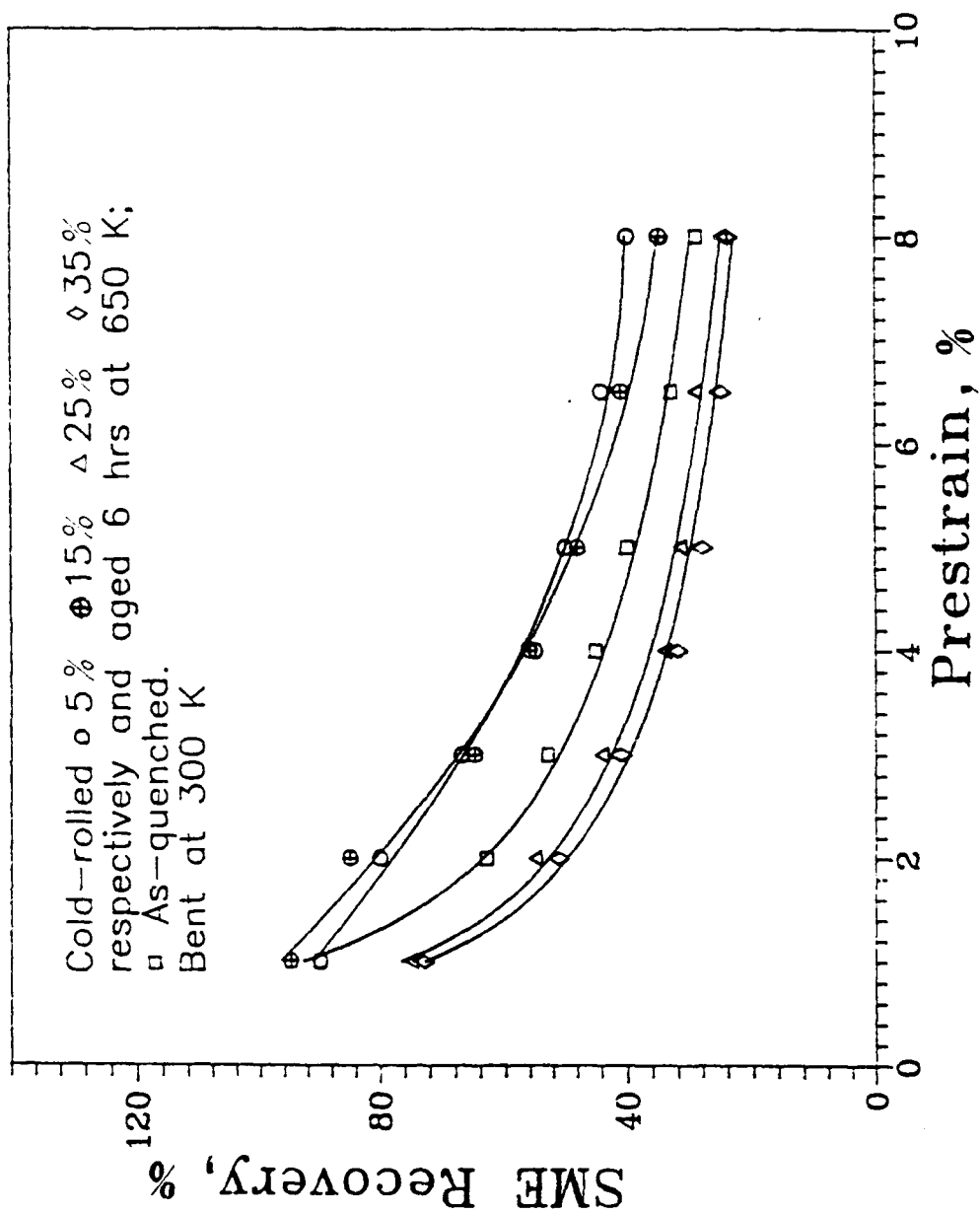


Figure 16. Effect of cold rolling on the shape memory strain recovery of alloy #3.

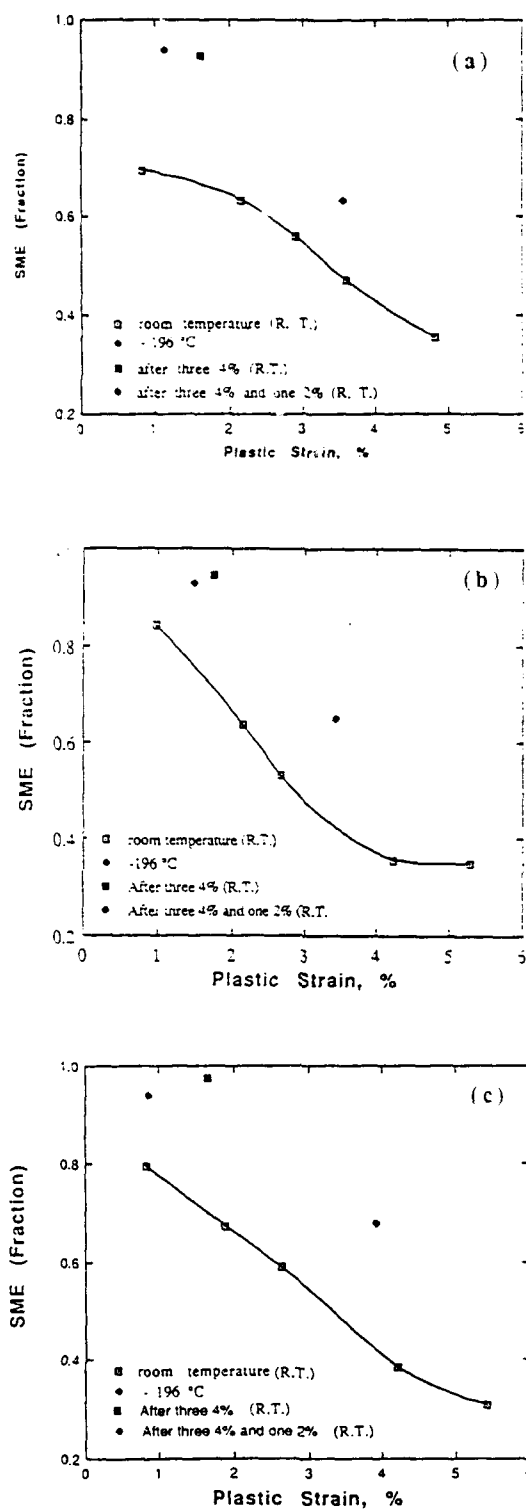


Figure 17. SME results of alloy #9 with different deformation temperature, strain and thermo-mechanical training, (a) water quenched, (b) aged at 700°C, (c) aged at 800°C.

curve shown in Figure 18a exhibits two-stage yielding typical of a shape memory alloy. The two-stage yielding curve is enlarged and shown in Figure 18b. Because the test sample is in fully martensitic condition, the first yielding which occurs at 396 MPa is associated with the realignment of martensite variant orientation. The alloy exhibits an excellent ductility of 65% before failure.

The yield stress of Fe-Mn-Si-Nb-C, determined by 0.2% offset, is plotted in Figure 19. Aging of the alloy at 700 and 800°C increases the strength of the alloy through the precipitation of NbC particle. The morphology of the precipitate is shown in the micrograph in Figure 20 where NbC particles are indicated by arrows.

1-d. Martensite Morphology and Shape Memory Mechanism

The fcc \rightarrow hcp martensitic transformation proceeds by the movement of $(a/6)\langle 11\bar{2} \rangle$ Schockley partial dislocations on every second $\{111\}$ plane of the fcc structure. Since there are four $\{111\}$ planes in the fcc structure, each having three $\langle 11\bar{2} \rangle$ directions, there is a total of 12 variants of transformation displacement. However, because the three $\langle 11\bar{2} \rangle$ directions are equivalent in crystallography, there are only four habit plane variants.

A single displacement variant of ϵ martensite plate with $(\bar{1}\bar{1}1)$ habit plane is shown in Figure 21. The plate intercepts with a (111) stacking fault, as indicated by an arrow, and generates a 19.5° displacement as described by the trace of ABCD. The displacement is consistent with the theoretical calculation based on a single $\langle 11\bar{2} \rangle$ shear operation. This type of ϵ martensite variant is often observed at an early stage of the transformation when the plate thickness is less than 150 nm.

Thicker ϵ plates tend to form with internal strain accommodation, as shown in Figure 22. The plate has a $(\bar{1}\bar{1}1)$ habit plane and intersects with several $(11\bar{1})$ stacking faults. Here, the intersections do not generate overall displacement of the (111) faults, indicating the absence of overall transformation displacement. The intersections inside the ϵ martensite plate leave behind serrated traces which is consistent with the geometry with all three $\langle 11\bar{2} \rangle$ variants present in a self-accommodating configuration. A perfect strain accommodation in a habit plane variant can occur when all three $[211]$, $[\bar{1}\bar{2}1]$ and $[\bar{1}\bar{1}\bar{2}]$ shear variants are present in equal thickness. An example of such a self-accommodating ϵ plate is shown in Figure 23 where line AE represents a trace of the original (111) plane. With no overall displacement present, the trace, however, is displaced into BC and CD inside the ϵ plate which consists of layers of three displacement variants. Line segment BC in V_1 variant forms an angle of 19.5° with the original AE trace. The angle between AE and the CD segment, which is a combination layer of V_2 and V_3 variants, is 8.5° . The two angles are in agreement with theoretical

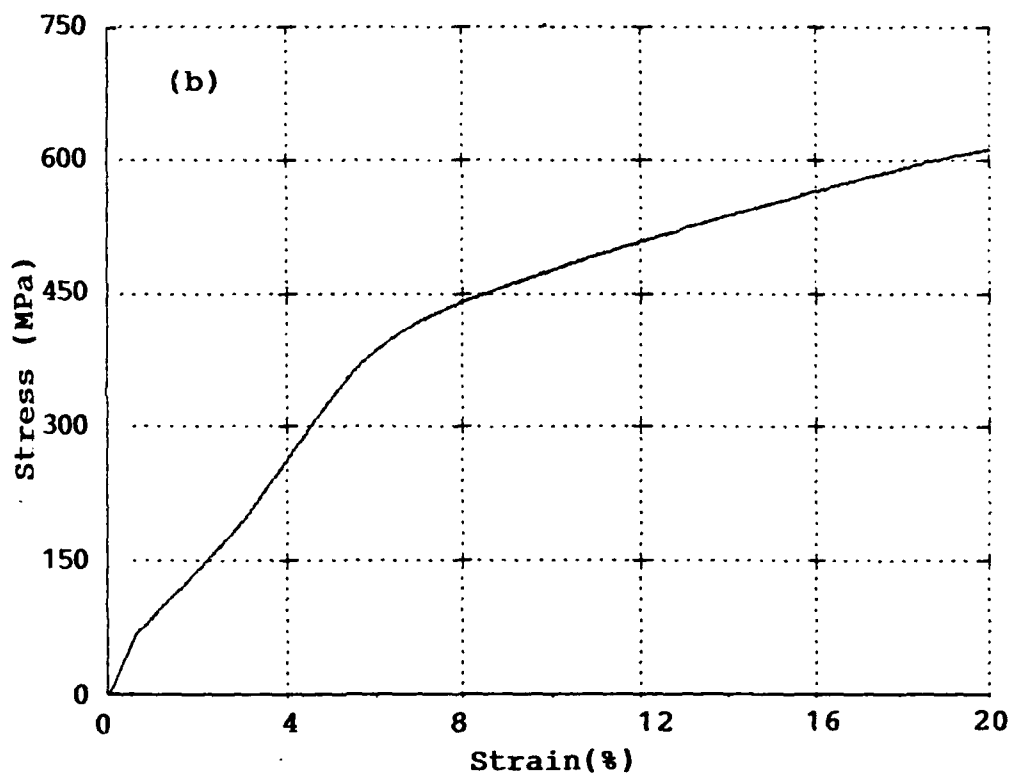
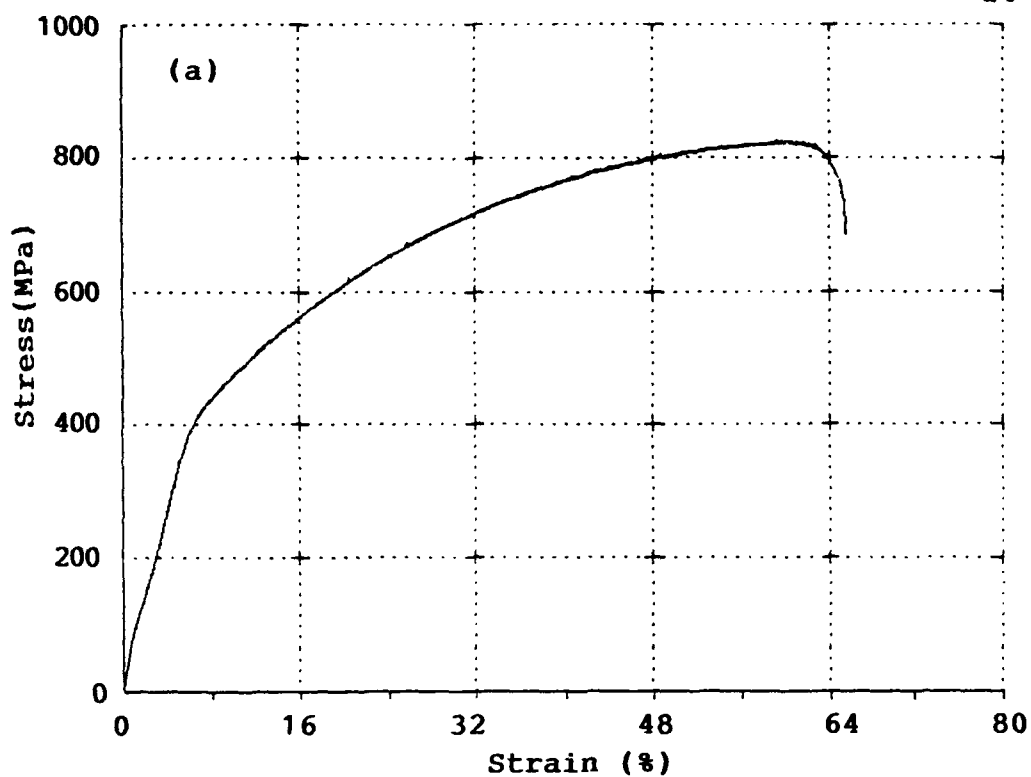


Figure 18. (a) A stress-strain curve of alloy #2 tested at 50°C after cooled to -196°C.
(b) The enlarged two stage yielding portion of (a).

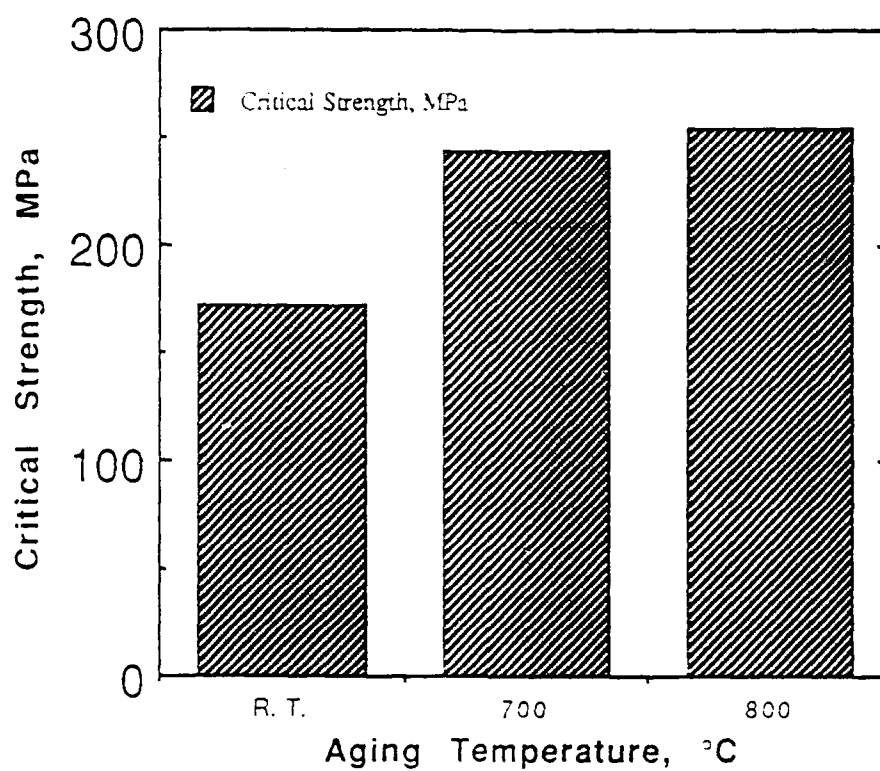


Figure 19. The yield stress of alloy #9 for different aging temperatures.

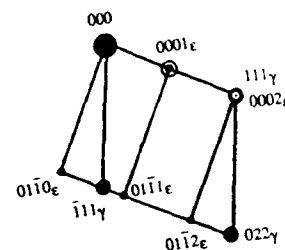
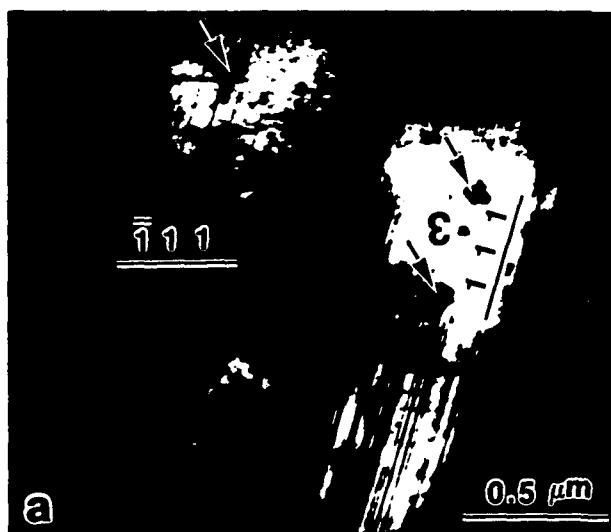


Figure 20. TEM view of alloy #9 aged at 800°C for 5 hrs. NbC precipitates are indicated by arrows.

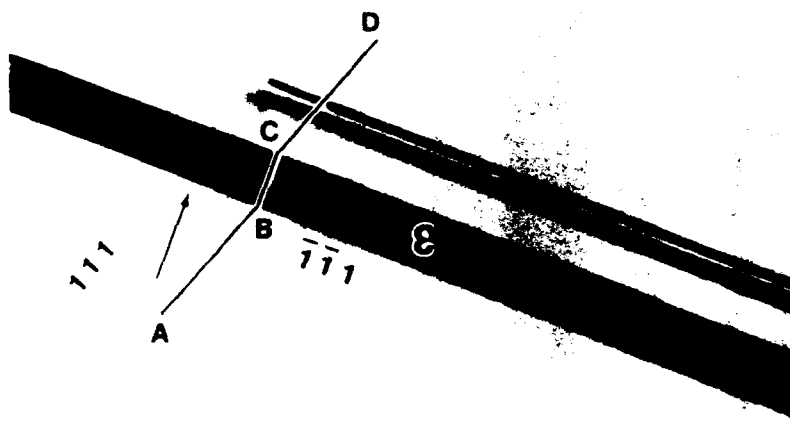


Figure 21. A single-variant band of martensite with (111) habit plane, from alloy #2.



Figure 22. Electron micrograph showing the internally self-accommodating bands of martensite.

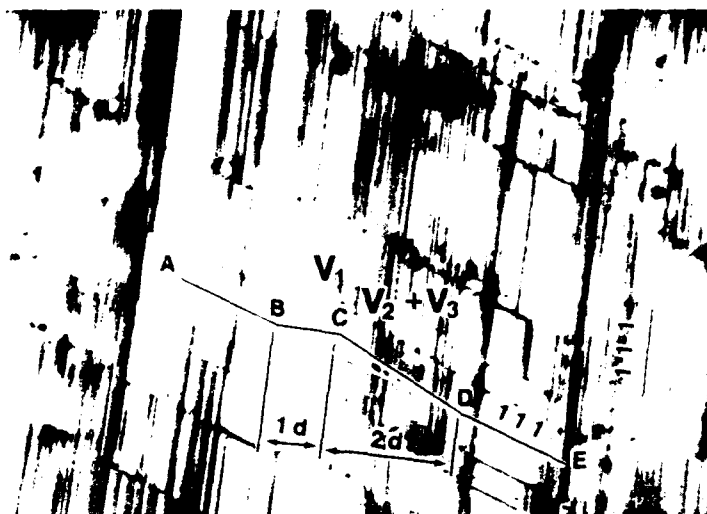


Figure 23. Strain accommodation among three shear variants of martensite of the same habit plane.

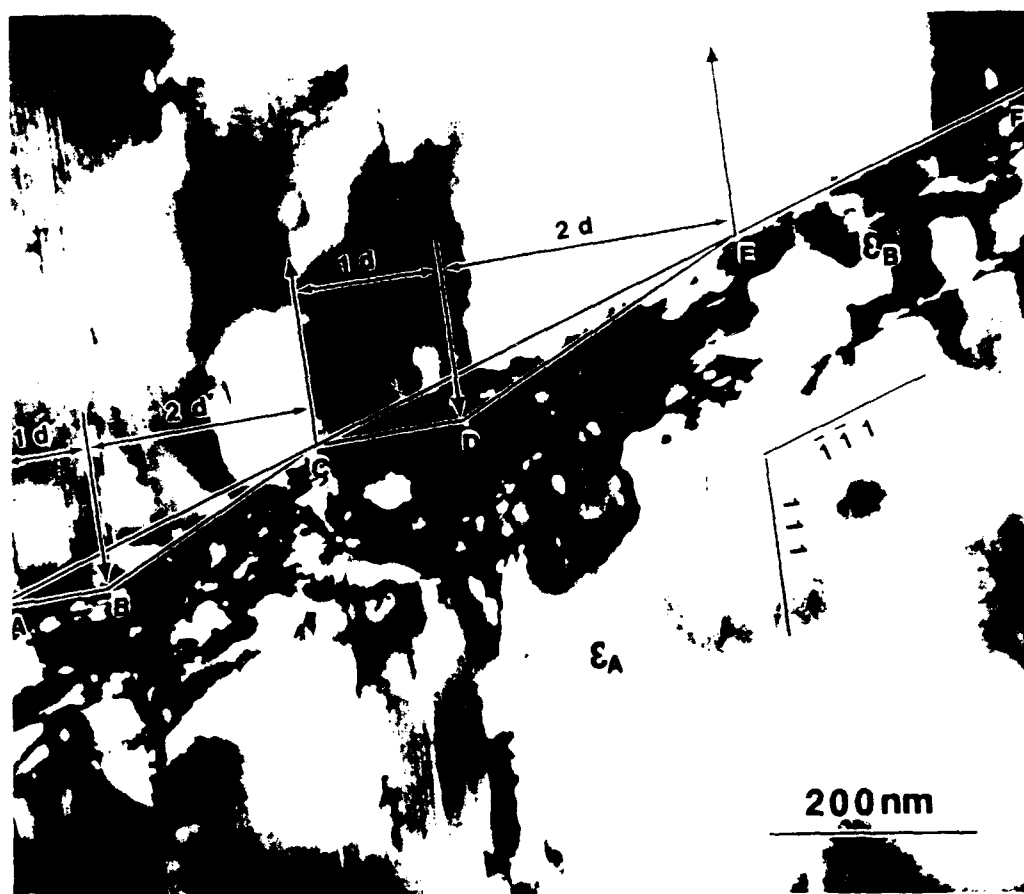


Figure 24. Strain accommodation among three shear variants of martensite of different habit planes.

calculations. The thickness ratio between V_1 and V_2+V_3 layers is 1:2, suggesting an equal volume ratio among the three variants.

Strain interactions between different habit plane variants are straight forward when each habit plane variant is self-accommodated. As shown in the micrograph of Figure 24, an even geometrical distribution of the three $\langle 11\bar{2} \rangle$ displacement variants generates the same serrated morphology at the plate intersection as in Figure 23. Again, the interaction creates no overall transformation displacement.

Similar to the mechanical effect in other shape memory alloys, deformation stabilizes primary displacement variants and generates macroscopic deformation. Figure 25 shows an intersection between variant V of (111) habit and variant ϵ of (11 $\bar{1}$) habit in a deformed specimen. The intersection displaces variant ϵ but not variant V, suggesting that variant V has a preferred shear variant even though the thickness is about 300 nm. This configuration of preferred displacement variant gives rise to a macroscopic strain and, upon reverse transformation, shape recovery. The processes of shape memory effect associated with ϵ martensite are illustrated schematically in Figure 26.

2. Fe-Ni-Ti-Co Alloys

2-a. Transformation Temperatures

The electrical resistivity curves of a Fe-33wt.%Ni-12wt.%Co-5wt.%Ti alloy after solution heat treatment and those after solution treatment and subsequent aging at 700°C for 5-30 hours are shown in Figure 27. No transformation was observed in the solution treated specimen. After aging at 700°C for 5 and 10 hours, transformations were observed during both cooling and heating. The transformation hysteresis is approximately 40°C, indicating that the transformation becomes thermoelastic. After aging for 30 hours, again, no transformation was observed. The transformation temperatures determined from the ER curves are listed in Table V.

Table V. Transformation temperatures (°C) of Fe-33wt.%Ni-12wt.%Co-5wt.%Ti after solution treatment and subsequent aging at 700°C.

Aging time	M_s	M_f	A_s	A_f
5 hours	-95	-148	-110	-30
10 hours	-85	-140	-75	-20

2-b. Shape Memory Effect

Perfect shape memory effect was demonstrated for the Fe-33wt.%Ni-12wt.%Co-5wt.%Ti after aging. Although only qualitative, the photographs in Figures 28 and 29 show the shape memory effect

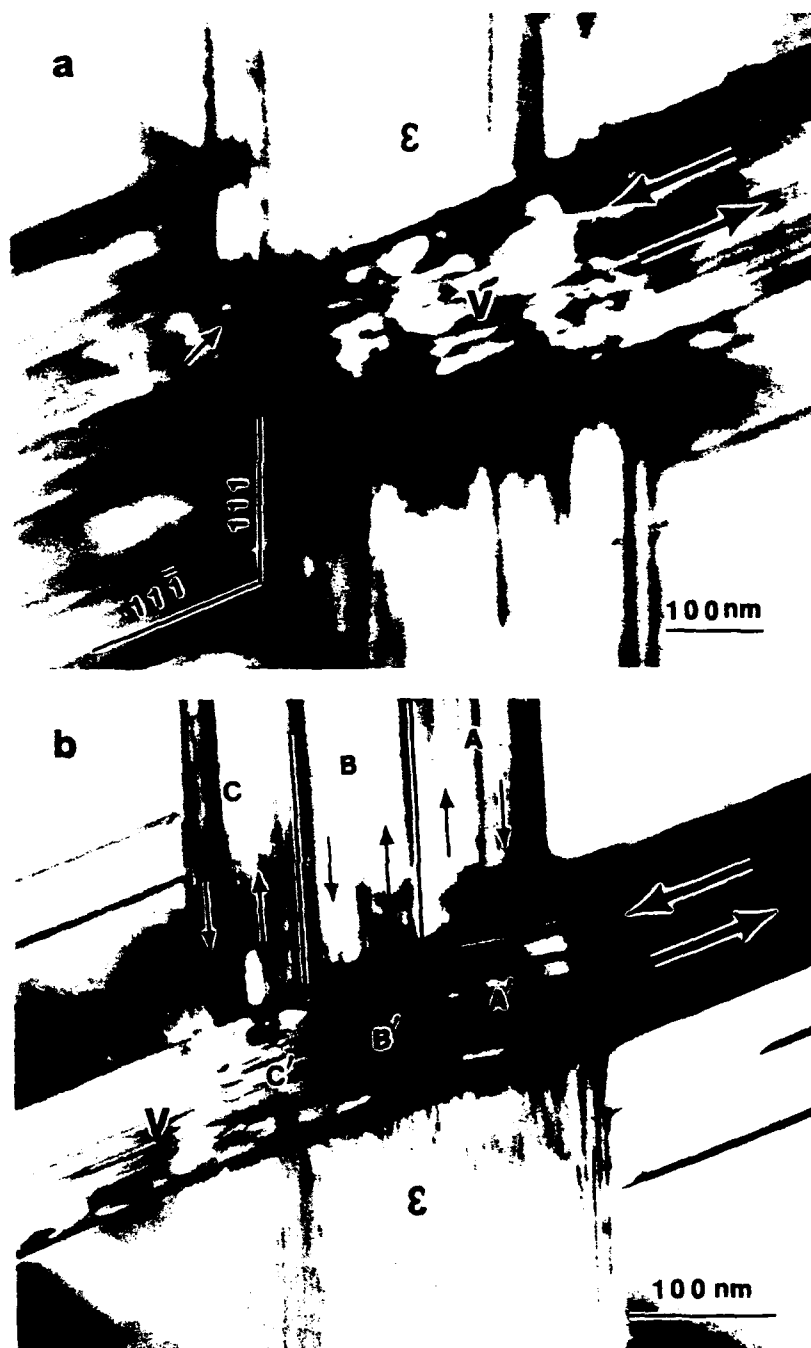


Figure 25. Electron micrographs showing the intersection of two martensite variants, showing a generally self-accommodating ϵ -band sheared by a presumably preferred variant V in a deformed specimen.

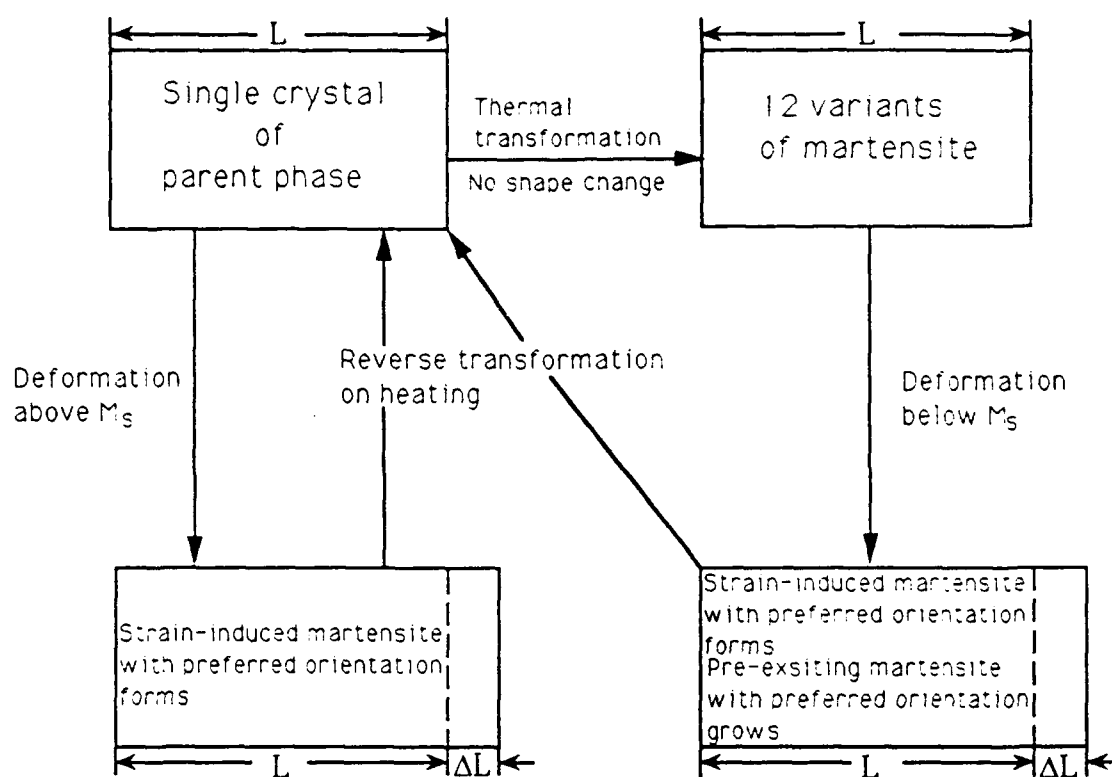


Figure 26. Schematic illustration of various processes involved in the shape memory effect associated with martensite transformation.

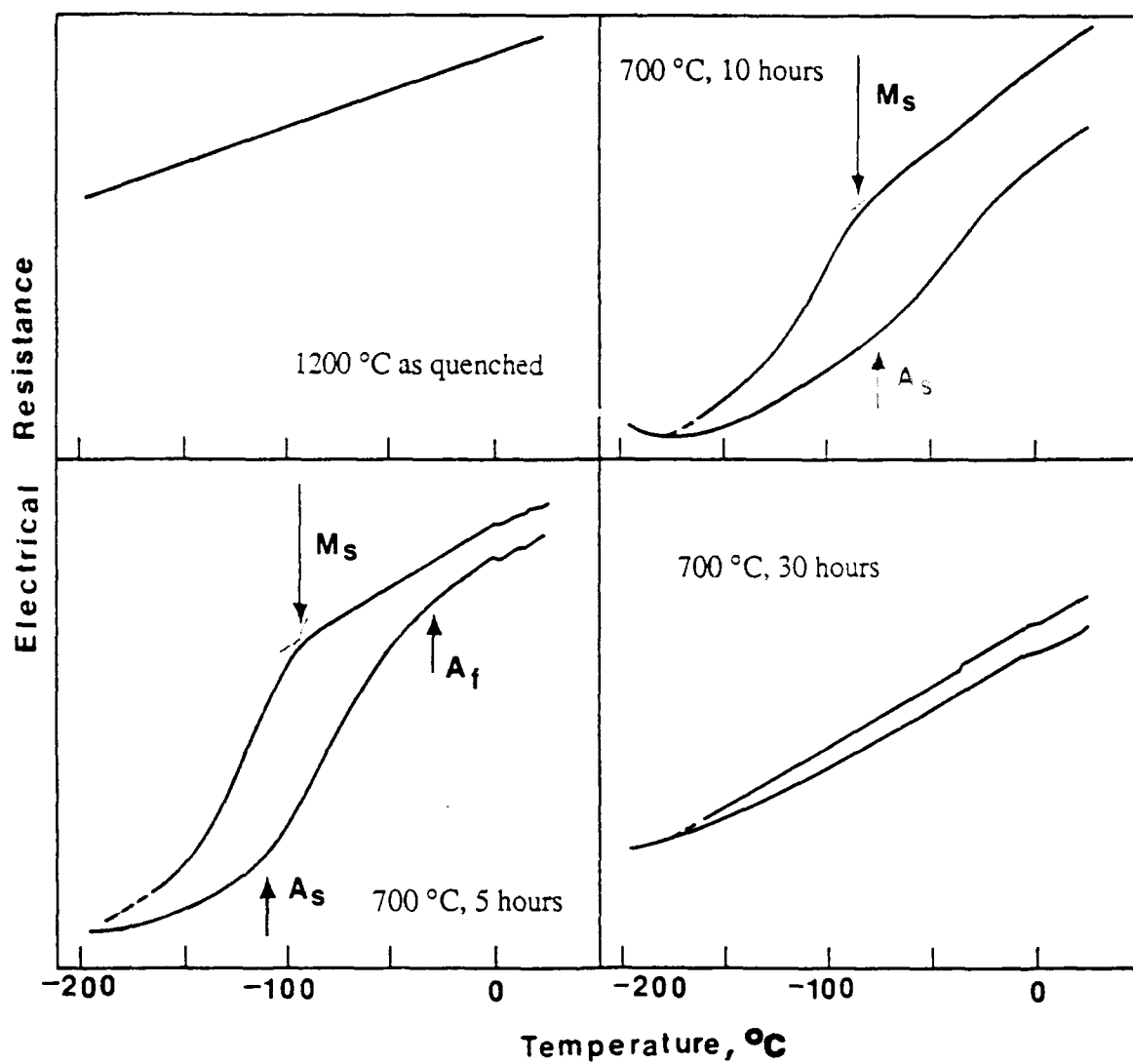


Figure 27. Electricity vs. temperature curves showing the effect of aging on martensite transformation of an FeNiCoTi alloy.

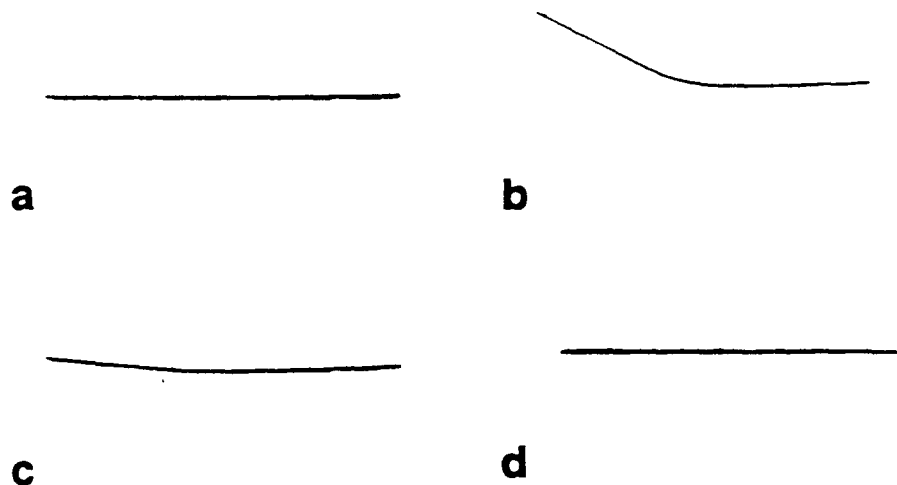


Figure 28. Shape memory effect of a specimen aged at 700°C for 5 hrs, (a) before bending, (b) after bending at -196°C, (c) after heating to 25°C, (d) after flame heating to above 700°C.

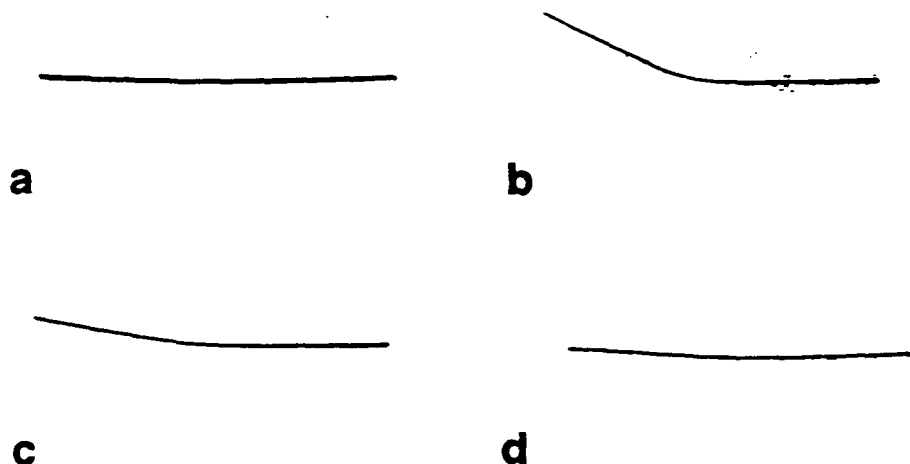


Figure 29. Shape memory effect of a specimen aged at 700°C for 10 hrs, (a), (b), (c) and (d) correspond to the same conditions as in figure 28.

in specimens after 700°C aging for 5 and 10 hours, respectively. Both specimens were first deformed at -196°C and subsequently heated to both ambient and 700°C. Both samples recover their original shapes after heating.

2-c. Microstructure and Martensite Morphology

Shown in Figures 30 (a), (b) and (c) are the micrographs of the alloy after aging at 700°C for 5, 10 and 30 hours, respectively. All three micrographs show the presence of spherical precipitate of Ni_3Ti γ' in austenite matrix. The size of the precipitate increases with aging time. The electron diffraction pattern in Figure 31 is a [011] zone pattern of the austenite and the precipitate. The pattern exhibits reflection spots originating from the precipitate which has an ordered fcc (Ll_2) crystal structure. The pattern suggests that γ' particles precipitate along the epitaxial orientation of the austenite. As expected in a martensitic transformation, the orientation relationship between the precipitate and the matrix is preserved after the martensitic transformation. This is demonstrated in a [110] zone pattern of the bct α' martensite in Figure 32.

Specimens of Fe-33wt.%Ni-12wt.%Co-5wt.%Ti after aging at 700°C for 5 and 10 hours contain both lenticular (LM) and thin plate martensite (TP) plates at room temperature, as shown in the micrographs in Figures 33a and b, respectively. Higher magnification micrographs of a thin plate and a lenticular martensite in specimens aged for 5 hours are shown in Figures 34 and 35, respectively. Both show the presence of γ' precipitate. The thin plate martensite does not have any fine structure while the lenticular martensite exhibits high density of transformation twin at the martensite midrib. Similar features were observed in martensites after aging for 30 hours (Figure 36).

The change in microstructure in a specimen aged for 10 hours is shown in a series of micrographs in Figure 37. Upon cooling to -110°C, the lenticular martensite remains stable while the thin plate martensites thicken with decreasing temperature. In addition, new plates of thermoelastic thin plate martensite also appear and grow.

On heating back to 60°C, most newly formed thin plate martensite reverse back to the austenite, although some residual plates remain even at 60°C. Pre-existing thin plate martensite, however, did not shrink on heating, suggesting that they are not reversible.

3. Fe-Al-C System

3-a. Martensitic Transformation Temperatures

An ER curve of a Fe-7wt.%Al-2wt.%C is plotted in Figure 38. During first cooling cycle, martensitic transformation is present in association with a drop in electrical resistivity between

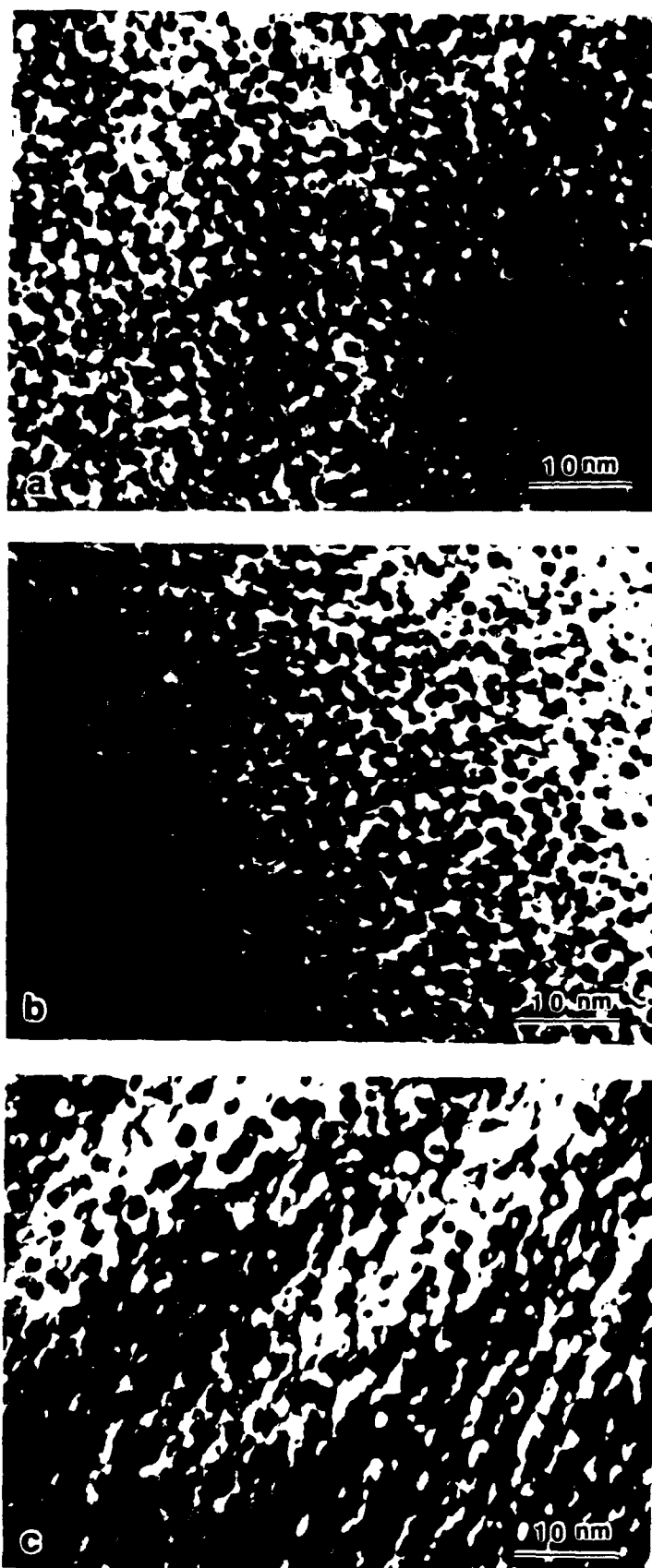


Figure 30. Electron micrographs of FeNiCoTi alloy aged at 700°C for (a)5, (b)10 and (c)30 hours.

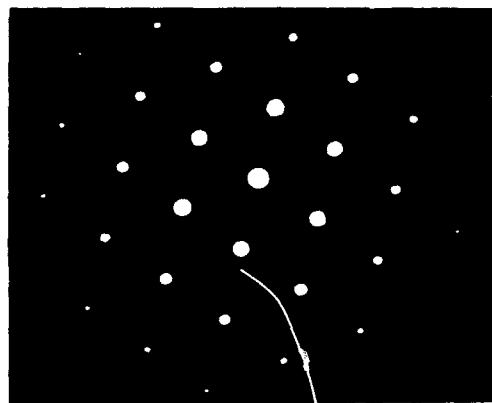


Figure 31. A $[011]$ zone electron diffraction pattern of the austenite and the Ni_3Ti precipitate phases.

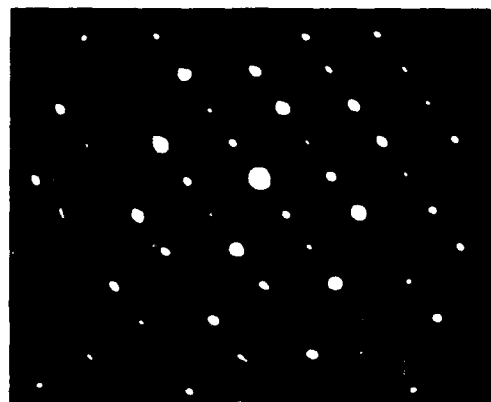
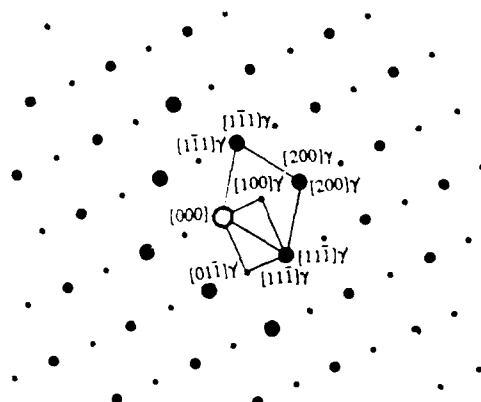
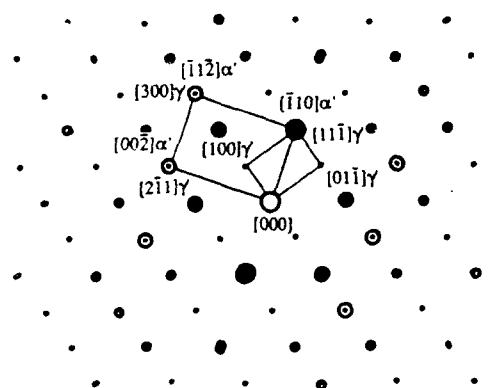


Figure 32. A $[110]$ zone electron diffraction pattern of the bct martensite and the Ni_3Ti precipitates.



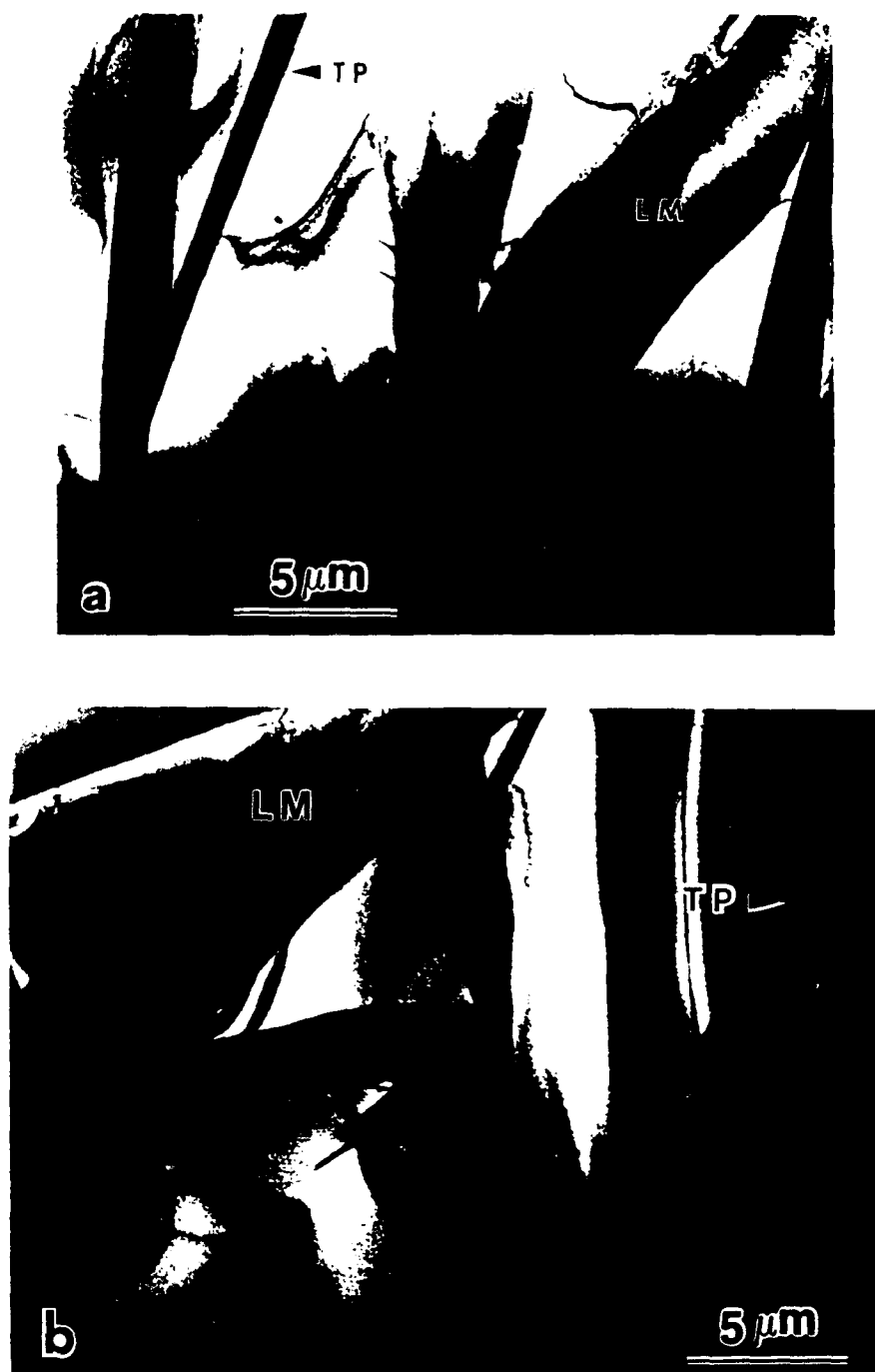


Figure 33. Electron micrographs of FeNiCoTi alloy after aging at 700°C for (a) 5 and (b) 10 hours, showing both lenticular (LM) and thin plate (TP) martensite morphologies.

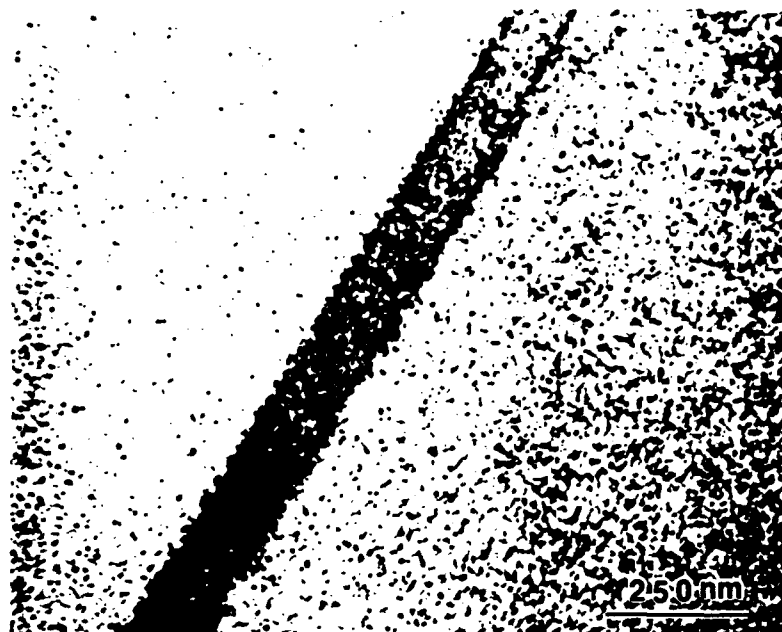


Figure 34. Electron micrograph of thin plate martensite in FeNiCoTi after aging at 700°C for 5 hours, showing no fine structures in martensite plate.

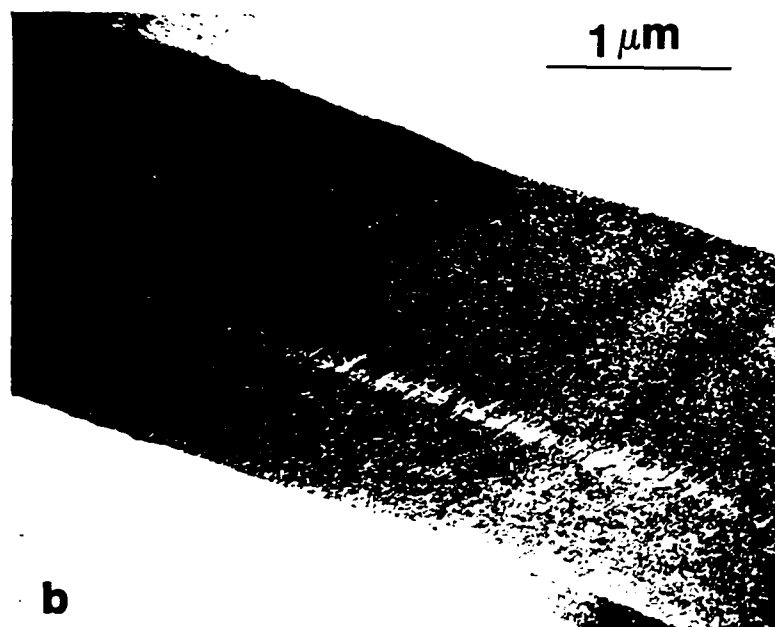


Figure 35. Electron micrograph of lenticular martensite in the same specimen as in Fig. 34, showing high density of transformation twin.

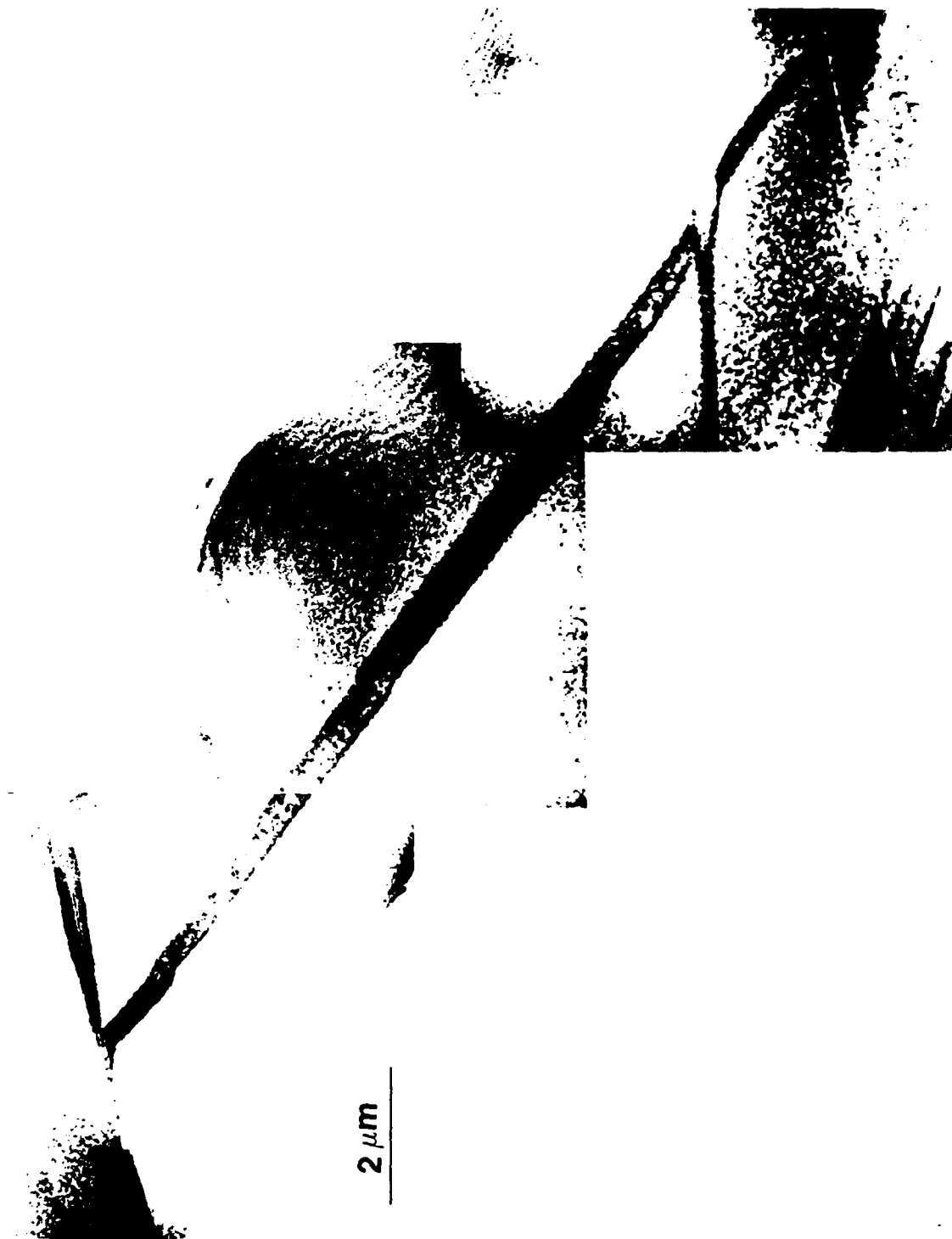


Figure 36. Electron micrograph of FeNiCoTi aged at 700°C for 30 hours.



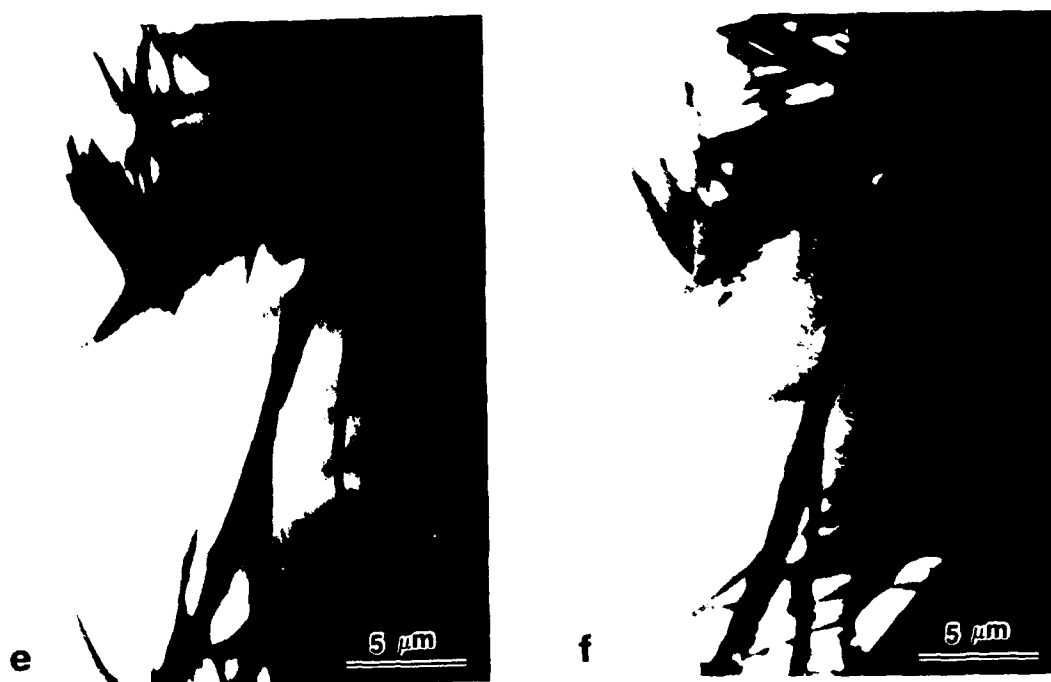


Figure 37. Microstructural change in FeNiCoTi aged for 10 hours, the specimen was cooled from 25°C (a) to -65°C(b) and -110°C(c) then heated to 0°C(d), 33°C(e) and 60°C(f).

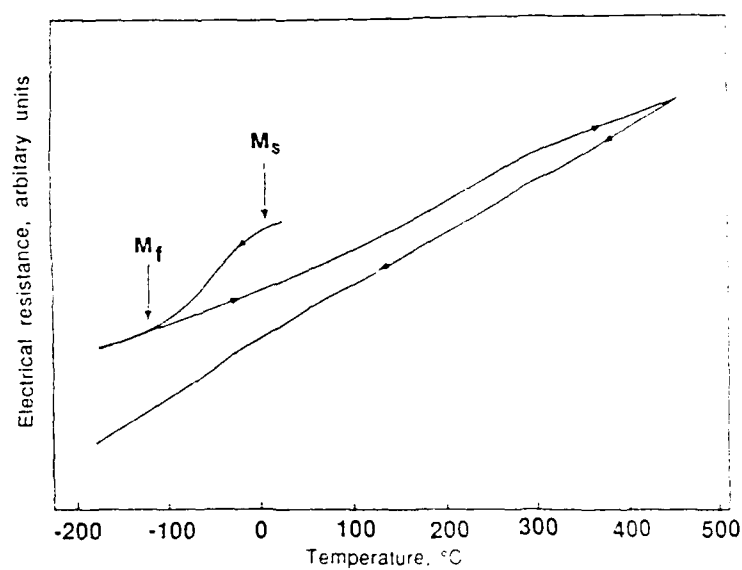


Figure 38. Electrical resistance change of Fe-7%Al-2%C with temperature showing M_s and M_f .

temperatures labelled M_s (0°C) and M_f (-120°C). Upon heating up to 450°C and subsequent cooling to -196°C , however, no transformation is observed.

3-b. Microstructure and Morphology of Martensite

The micrograph in Figure 39a shows the morphology of martensite after cooling to -45°C , typical of thin plate martensite. The microstructure of martensite after heating to 450°C contains a high population of carbide precipitate, a micrograph of which is shown in Figure 39b. The microstructure is typical of a tempered martensite.

3-c. Mechanical and Shape Memory Properties

Mechanical testing has been performed on the alloy. However, the alloy exhibits no ductility. The brittleness and the irreversible nature of martensite due to the carbide precipitation prevent the alloy from being an acceptable shape memory alloy.

4. Damping Properties

4-a. Fe-Mn-Si-Ni-Cr Alloy

The loss factor of Fe-Mn-Si-Cr-Ni (alloy #2) after solution treatment and subsequent aging at 300°C for 2 hours was determined using DMTA in a single cantilever mode at 137 microstrain and a frequency of 1 Hz. The results of the following sequence of tests are plotted in Figures 40 and 41.

- MM12AA - Scanned at $3.5^\circ\text{C}/\text{min}$ from 25 to 200°C .
- MM12AB - Measured damping at 35°C for 7 minutes.
- MM12AC - Scanned at $4^\circ\text{C}/\text{min}$ from 25 to 200°C .
- MM12AD - Measured damping at 50°C for 1 hour.
- MM12AE - Scanned at $4^\circ\text{C}/\text{min}$ from 35 to 200°C .
- MM12AF - Measured damping at 50°C for 1 hour.
- MM12AI - Isothermal from -40°C to 70°C with 10°C steps and 10 minute soak time.
- MM12AJ - Isothermal from -40°C to 200°C with 10°C step and 10 minute soak time.

The peak temperature of the loss factor corresponds very well to the reverse martensitic transformation temperature of the alloy. The first run shows a lower peak value of loss factor than on the second and the third runs, suggesting that mechanical cycling gives rise to higher damping, probably due to an interaction between martensite interfaces and dislocations generated during mechanical cycling. At temperatures below 80°C , all runs are virtually identical. These results suggest that the loss factor measurement is reproducible whether taken on rising temperature or under isothermal condition and the data is stable in the transition region after the first run. The difference between MM12AA and



Figure 39. (a) Martensite morphology of FeAlC after cooling to -45°C . (b) The microstructure of same alloy after heating to 450°C , showing a high carbide precipitate population.

MEMRY METALS SAMPLE 1-2A LOSS FACTOR AS A FUNTION OF
TEMPERATURE FOR THE FIRST SIX RUNS.

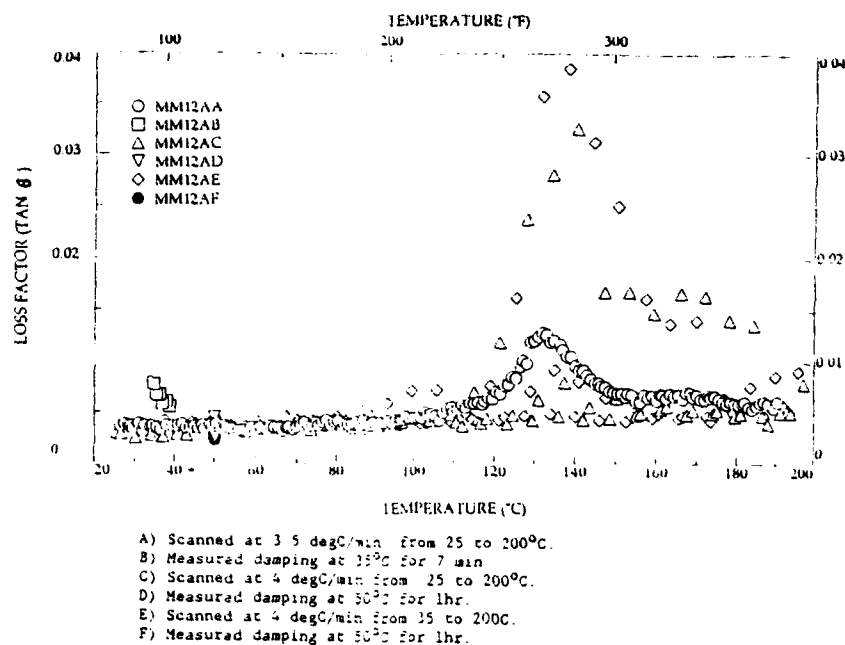


Figure 40. Loss factor of alloy #2 measured by DMTA at 1 Hz, two scan rate are used.

MEMRY METALS SAMPLE 1-2A LOSS FACTOR AS A FUNTION OF
TEMPERATURE FOR RUNS A, I AND J.

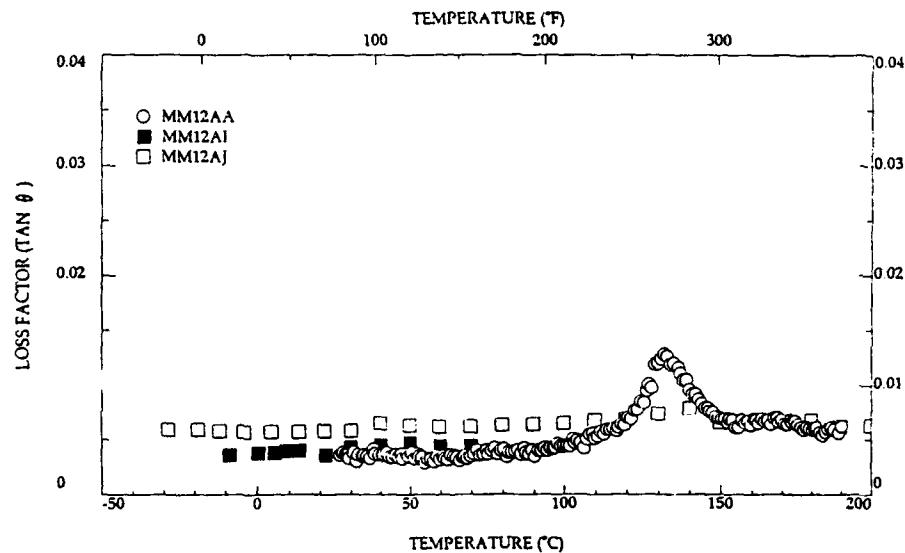


Figure 41. Loss factor of alloy #2 measured by DMTA at 1 Hz, isothermal data comparing with scanned data.

MM12AC also suggests that damping is probably scan-rate dependent.

Figure 42 shows the loss factor plotted against the storage modulus. The data for run A is typical for scan runs through a transition where the modulus does not decrease, i.e., NiTi. Runs C and E show the same tendency but with greater data scatter. Runs I and J are isothermal step runs. Run I agrees with other runs very well while the data from run J shows slightly higher damping, possibly due to mechanical fatigue.

The peak loss factor for the alloy is around 0.04 which corresponds to 25% SDC according to the following equation. This indicates that the alloy can be classified as a high damping alloy.

$$\text{SDC (\%)} = 200\pi \tan \theta$$

The strain amplitude dependence of the loss factor of the following two runs is plotted in Figure 43.

MM12AG - Measure damping at 50°C from 49 to 1100 microstrain after heating to 200°C.

MM12AH - Measure damping at 50°C from 49 to 1100 microstrain after cooling to -40°C.

Both runs show identical positive strain amplitude dependence, as expected from a mechanism related to martensite interface damping.

Testing at the University of Maryland was run at a frequency of 250 Hz and a strain amplitude range of 10-1000 microstrain. Samples after solution treatment and subsequent aging at 300°C for 2 and 24 hours were tested and the results are plotted in Figure 44. The internal friction peaks after aging at 300°C become more pronounced than those of solution treated sample. Several internal friction peaks are present after 300°C aging. The peak in the temperature range of 120-180°C is consistent with the DTMA result and is a result of the transformation. Other peaks present in the temperature range are probably related to other mechanisms that are frequency-dependent. Similar to the DTMA results, the sample after transformation thermal cycling exhibits more pronounced internal friction peaks as plotted in Figure 45, suggesting that transformation cycling also induces defects which enhance the damping effect.

The strain amplitude dependence of the damping was also investigated using the resonance technique. As shown in Figures 46-48, as the drive amplitude increases from low (10^{-5}) to average (5×10^{-5}) to high (10^{-3}), the internal friction peak shifts to lower temperatures. A series of the resonance curves corresponding to Figure 48 is plotted in Figure 49. The high damping is associated with highly pronounced nonlinearity, typical of an interface damping effect.

MEMRY METALS SAMPLE 1-2A LOSS FACTOR AS A FUNCTION OF STORAGE MODULUS FOR ALL RUNS.

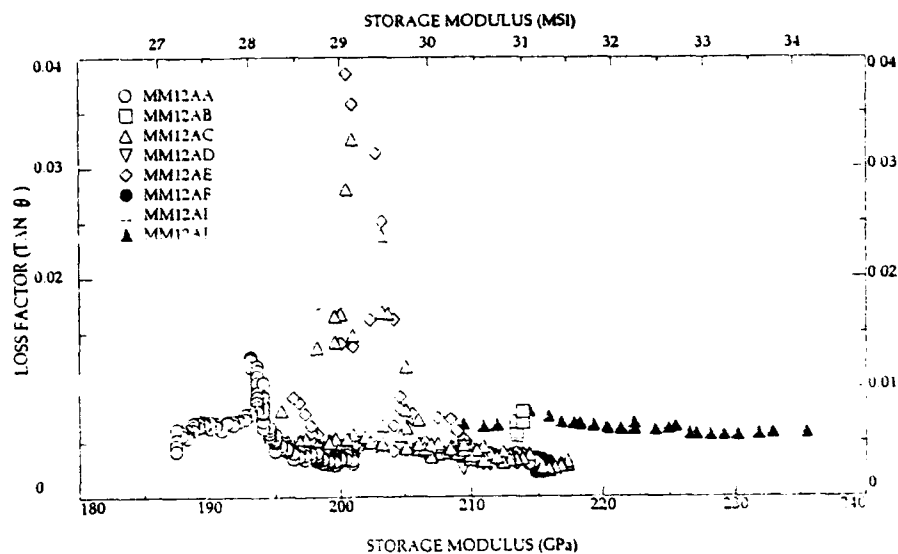


Figure 42. The loss factor-storage modulus relations for isothermal and scanned runs.

MEMRY METALS SAMPLE 1-2A LOSS FACTOR AS A FUNCTION OF STRAIN AMPLITUDE AT 50°C AND 1 HZ.

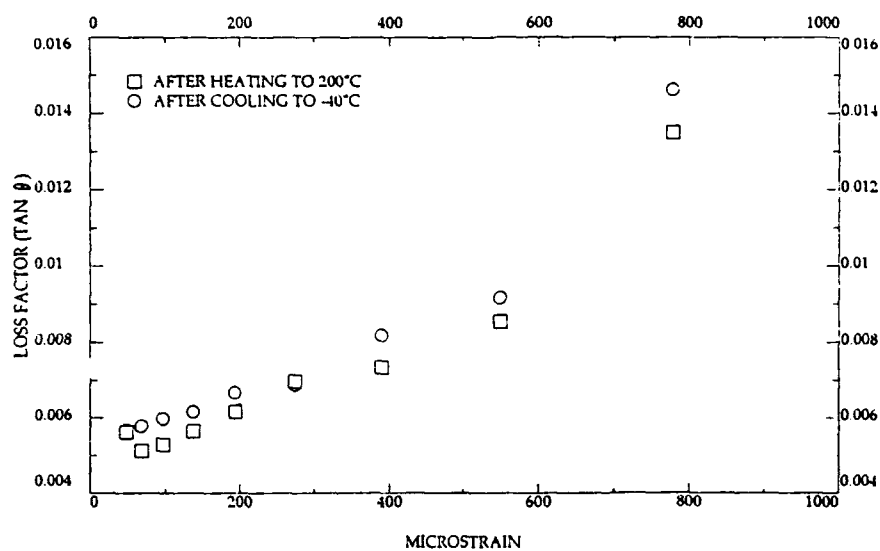


Figure 43. Strain amplitude dependence of the loss factor after different heat treatment.

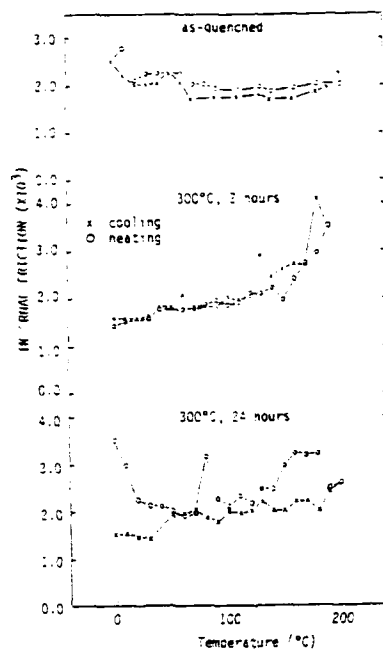


Figure 44. Internal friction-temperature relations for alloy #2, showing the aging effect.

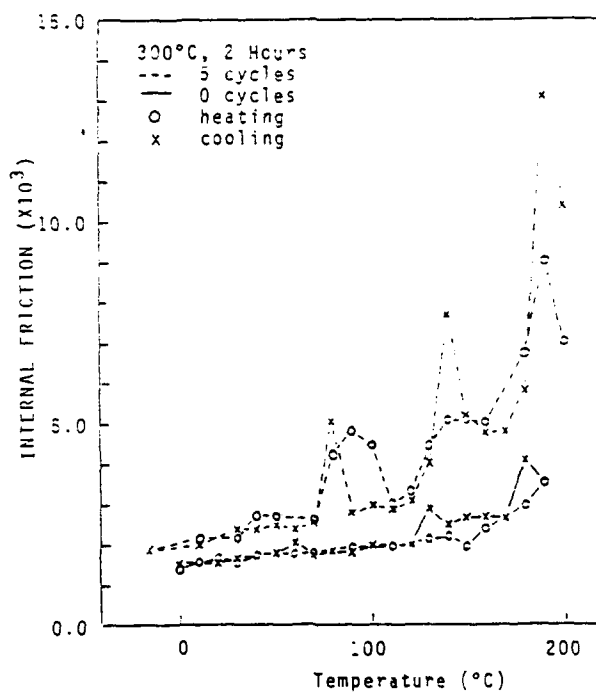


Figure 45. Internal friction-temperature relations for alloy #2, showing the thermal cycling effect.

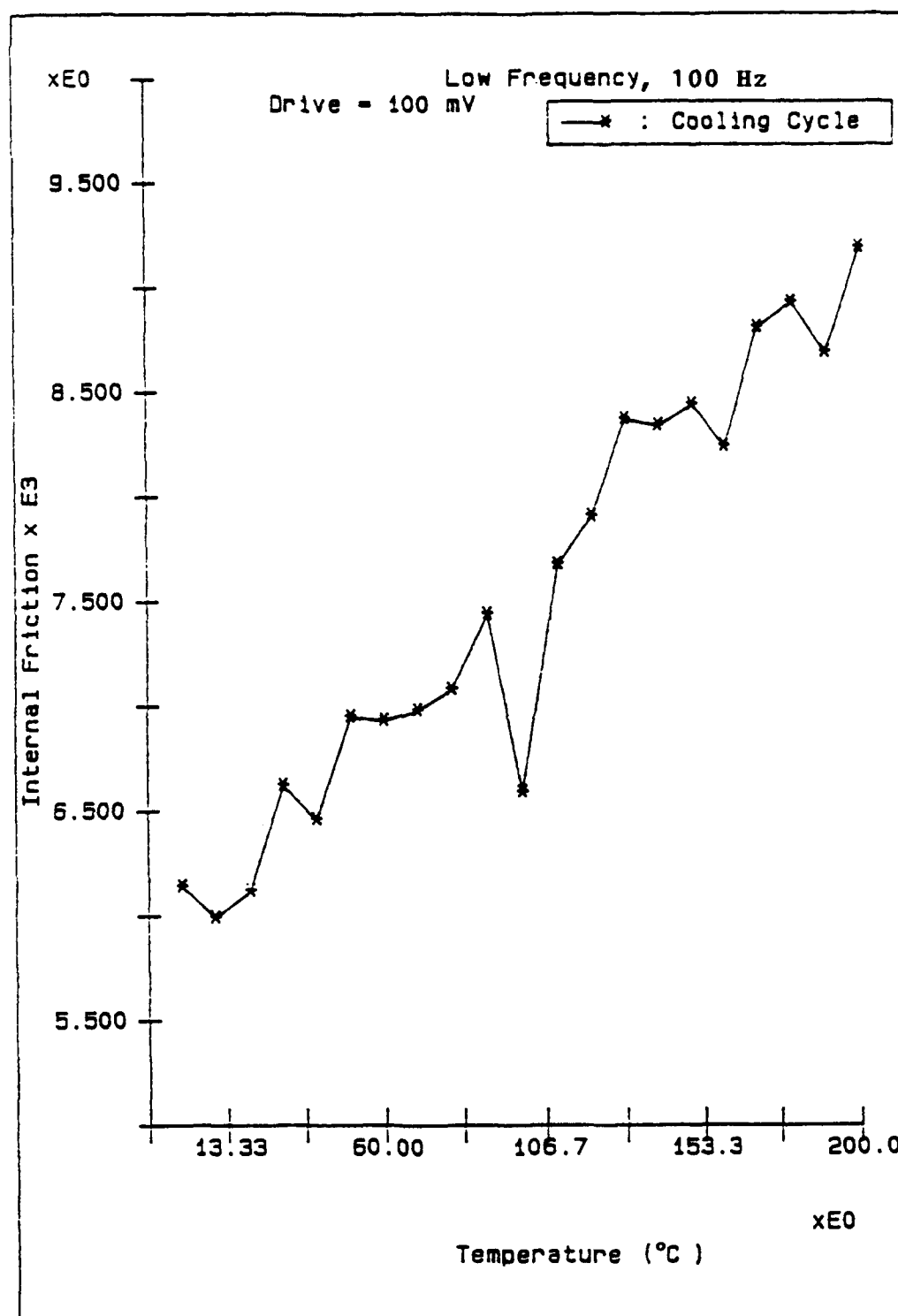


Figure 46. The change of internal friction with temperature for alloy #2, strain amplitude around 10^{-5} .

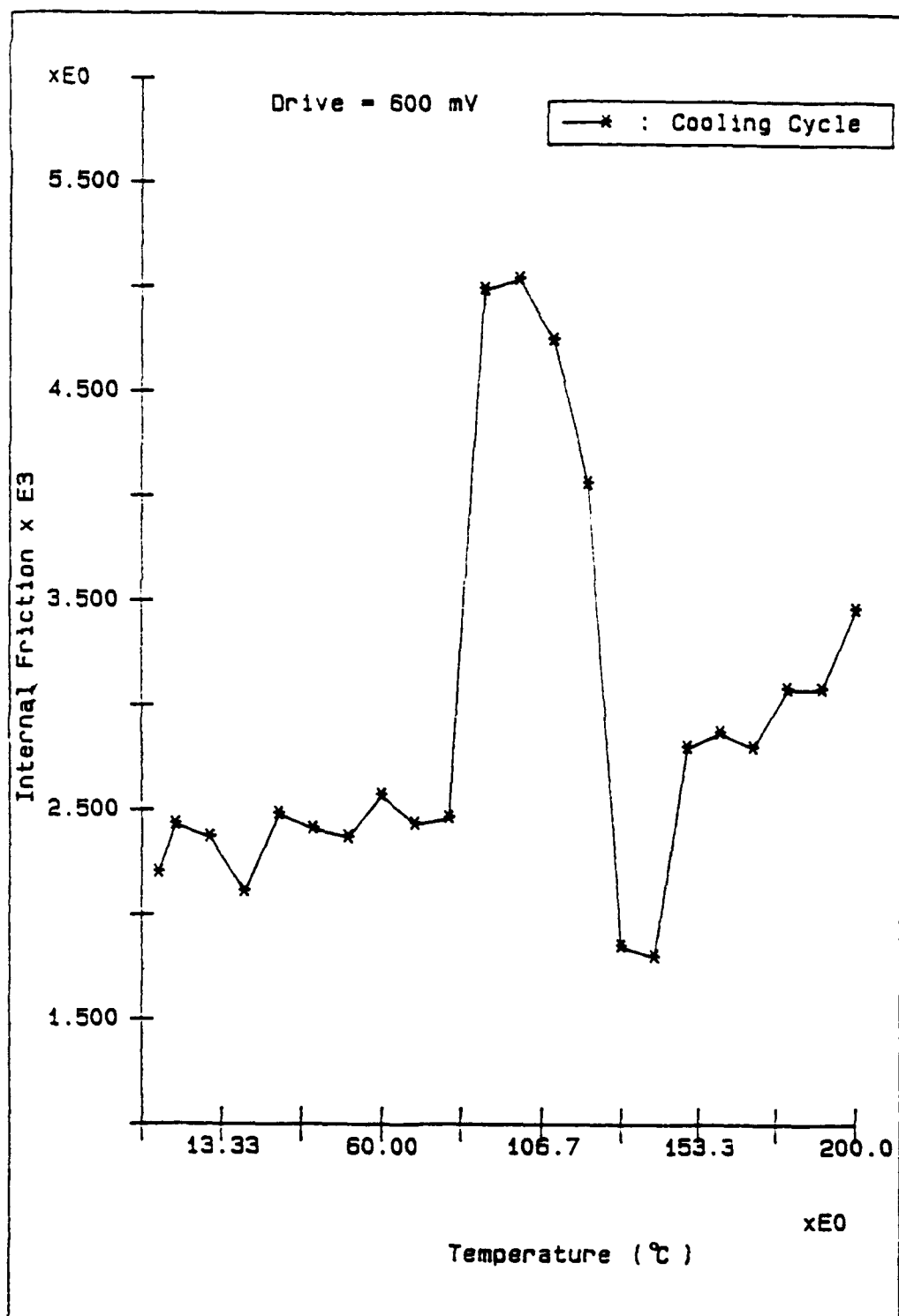


Figure 47. The change of internal friction with temperature for alloy #2, strain amplitude around 5×10^{-5} .

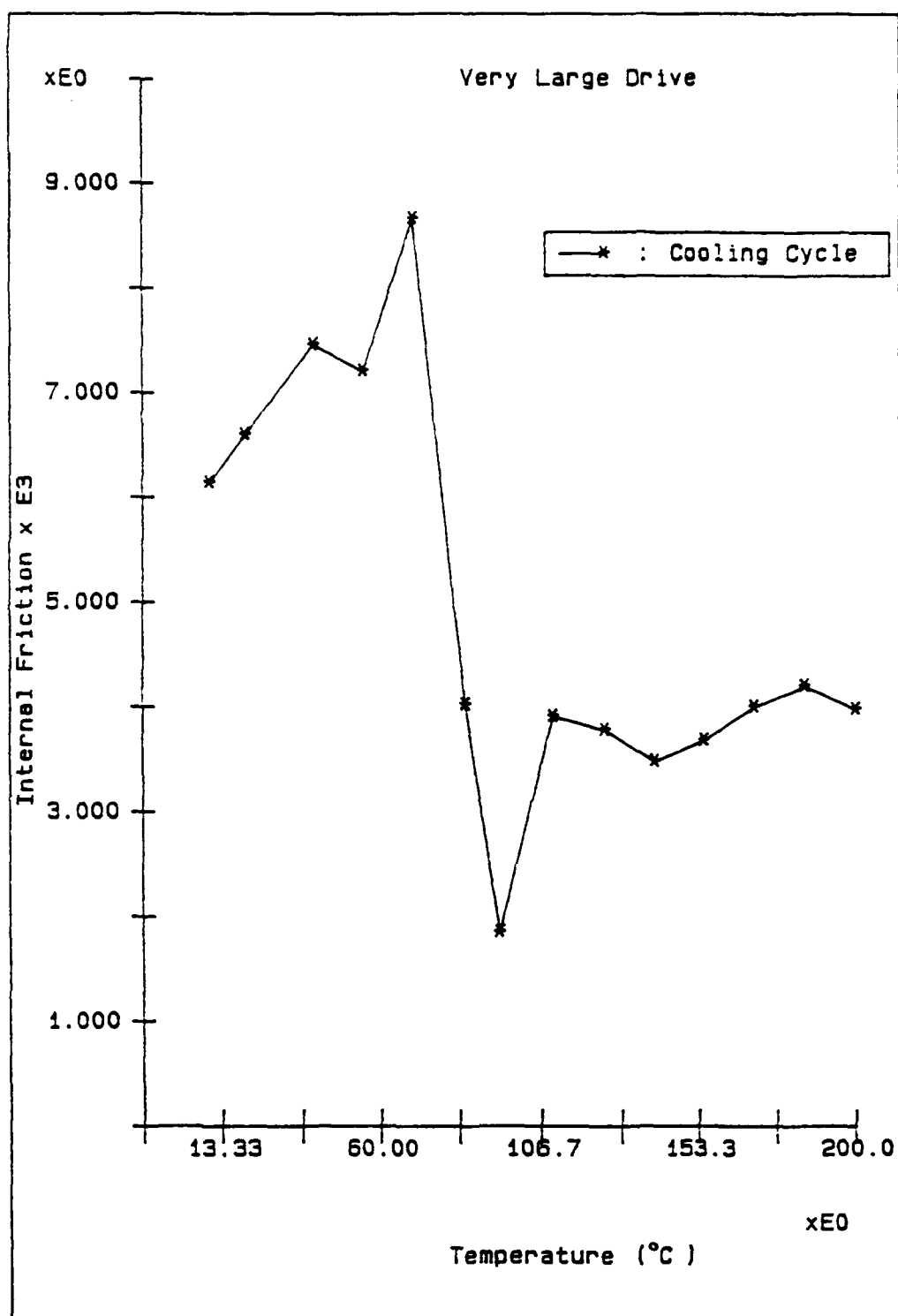
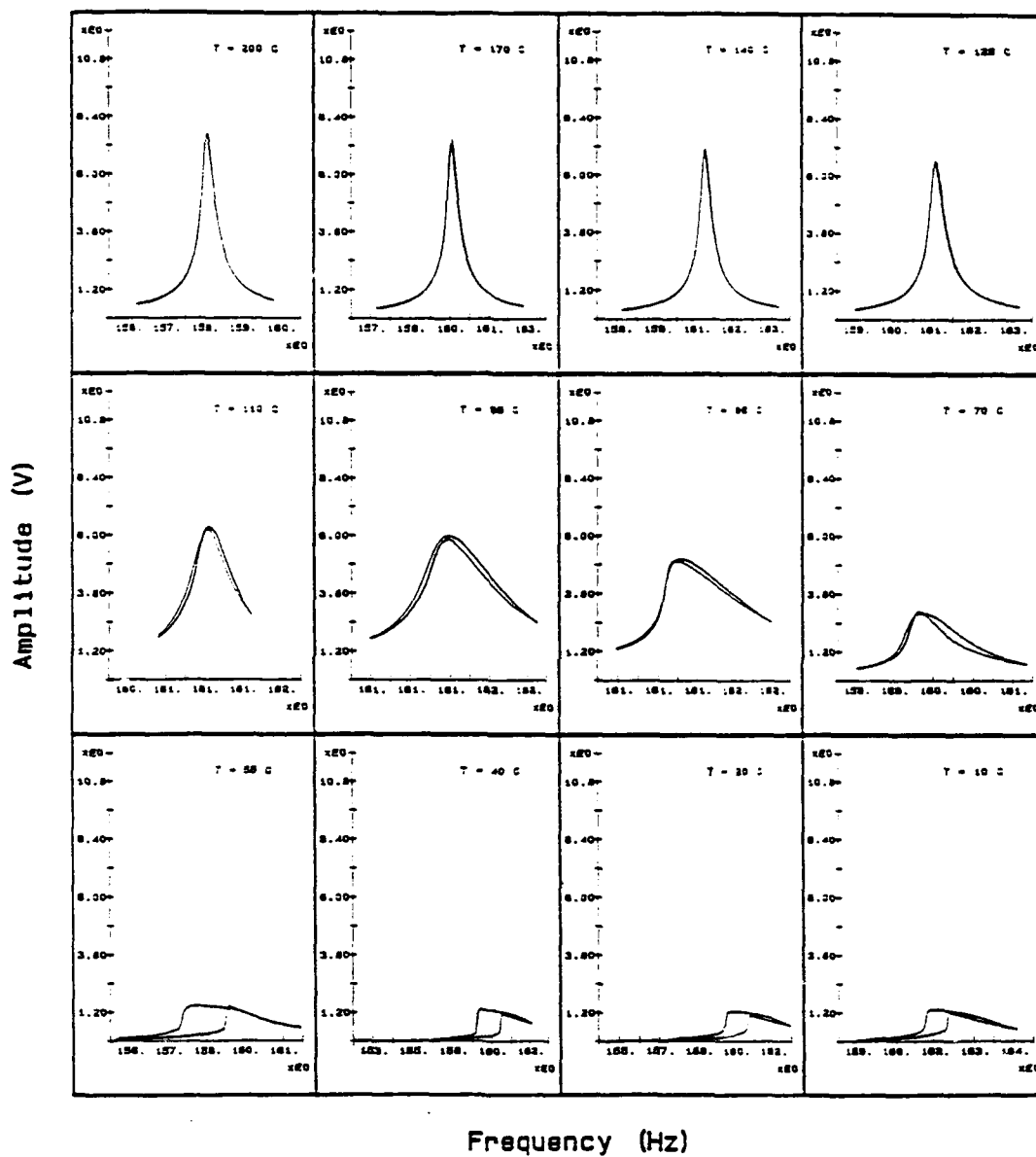


Figure 48. The change of internal friction with temperature for alloy #2, strain amplitude around 10^{-3} .

Alloy : Fe-Mn-Si-Cr-Ni*



* Cooling Cycle

Figure 49. The resonance curves corresponding to Fig. 48, showing pronounced nonlinearity as the M_s is approached.

4-b. Fe-Ni-Ti-Co Alloy

Damping of a Fe-33wt.%Ni-12wt.%Co-5wt.%Ti alloy in the as-solution-treated condition and after 700°C aging for 2 and 5 hours was measured using a resonance technique. The samples were first cooled to -185°C and then the damping was measured on heating. The results are plotted in Figure 50. Only a small damping peak is observed at approximately -20°C (253K) from the as-solution treated specimen. Specimens aged at 700°C exhibit a much higher damping plateau at temperatures below -110°C. The temperature corresponds well to the M_s temperature of the sample aged at 700°C for 5 hours. Both levels of damping associated with the -20°C peak and the low temperature plateau increase with aging time, but are lower than that of Fe-Mn-Si-Ni-Cr alloy. The alloy also exhibits softening in modulus with decreasing temperature. An example is shown in Figure 51 where the square resonance frequency, which is directly proportional to the Young's modulus, vs. temperature curve exhibits a minimum at approximately the A_s temperature.

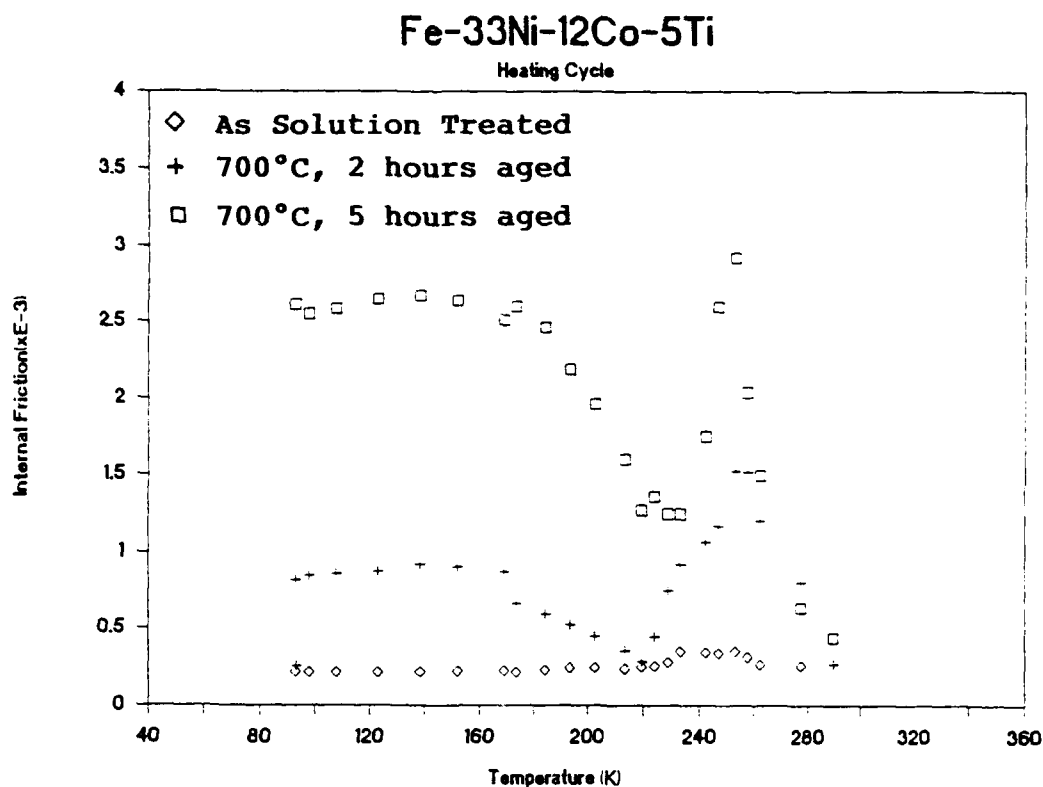


Figure 50. Internal friction-temperature relations of specimens with different aging treatments.

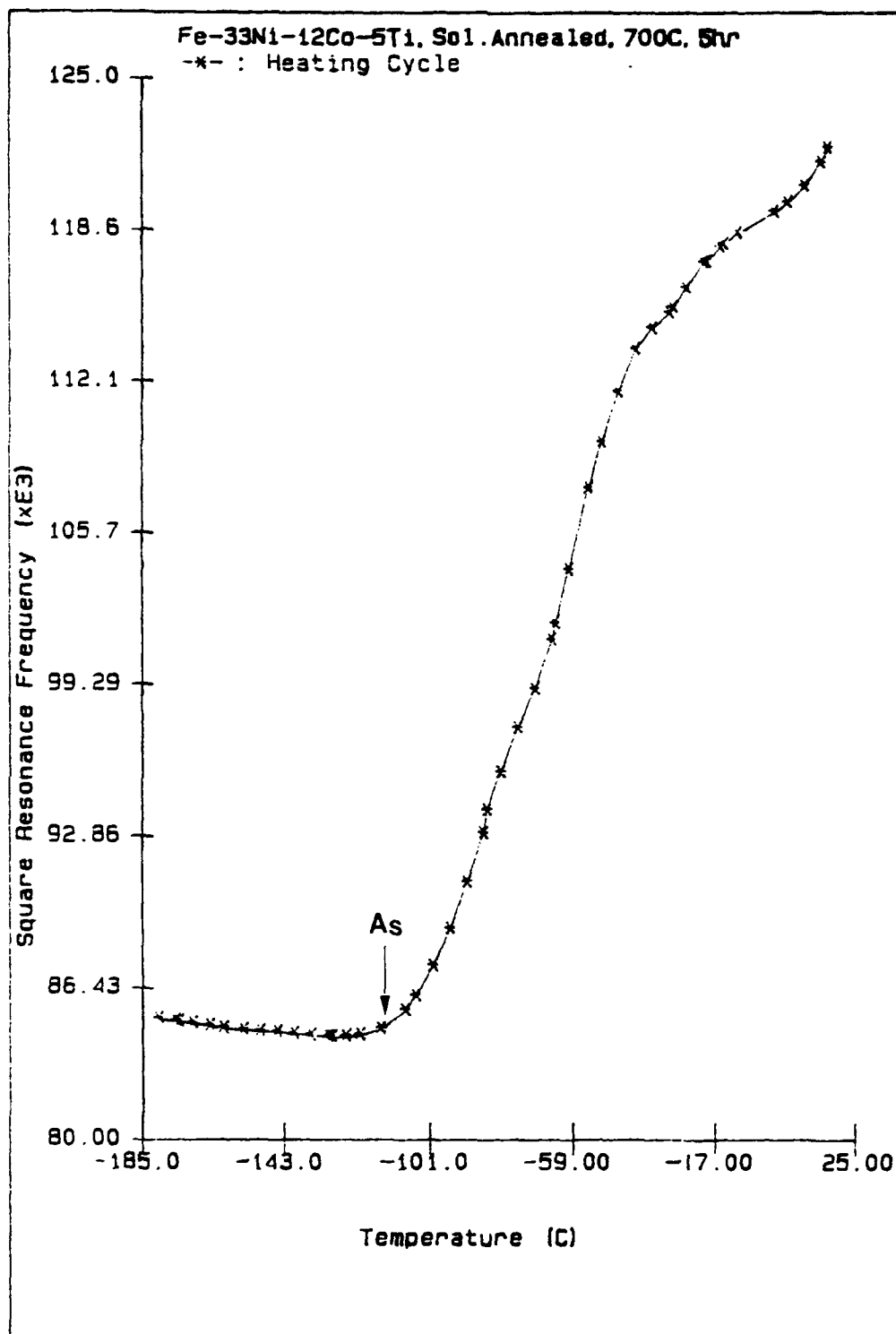


Figure 51. Change of the square resonance frequency with temperature, the minimum at A_s corresponds to the modulus minimum.

IV. DISCUSSION

1. Shape Memory Effect of Ferrous SMA

Among the three modified Fe-Mn-Si alloys studied, alloy #2 exhibits the same shape recovery whether the deformation was carried out at ambient temperature or liquid nitrogen (LN_2) temperature (-196°C). The other two alloys show a better shape recovery when deformed at LN_2 temperature than at ambient temperature. This behavior appears to be related to their antiferromagnetic transition which suppress the martensitic transformation. As indicated by their resistivity curves, alloys #3 and #9 require deeper cooling to induce sufficient amount of martensite for good shape memory effect.

The study of processing effects on the shape memory strain recovery suggests that proper thermomechanical treatments can improve shape recovery of Fe-Mn-Si-Ni-Cr alloy. These thermomechanical processes include transformation cycling, and a combination of proper cold work and annealing; both are expected to strengthen the matrix by the introduction of defects. This is again observed in Fe-Mn-Si-Nb-C system as the aging treatment induces NbC precipitation and raise the yield strength of the matrix (Figure 19). However, all these effects are only marginal as compared to conventional shape memory alloys, such as NiTi. A possible explanation is that work hardening and precipitation hardening are probably less effective in non-ordered fcc alloys (Fe-Mn-Si-X) than in ordered bcc alloys (NiTi).

Another reason that Fe-Mn-Si-X systems exhibit inferior shape memory strain recovery as compared to NiTi or Cu based alloys can also be explained from the nature of their variant distribution. The $\gamma \rightarrow \epsilon$ transformation generates only 12 variants as compared to 24 in conventional shape memory alloys. Instead of forming self-accommodating groups, the habit plane variants of ϵ martensite intersect with each other. The interaction between the $[112]$ slip in general generates a sessile structure such that the coalescence of variants during deformation in the martensitic structure is limited to those shear variants within the habit plane variant group (Figure 25).

Wider transformation hysteresis and transformation temperature span are indications of the less thermoelastic nature of the ϵ martensite as compared to the transformation in conventional shape memory alloys.

The effect of strengthening of γ matrix is demonstrated also in Fe-Ni-Ti-Co alloy through the precipitation of coherent Ni_3Ti γ' particles. The precipitate facilitates thermoelastic thin plate martensitic transformation. The crystallographic and morphological nature of the precipitate appears to be critical to the effect of precipitation. When the precipitate grows after over aging, the

transformation lose thermoelasticity.

The Fe-Al-C alloy lacks satisfactory mechanical properties to be a viable shape memory alloy. Present study suggests that high C alloy is less likely to be thermally stable as the precipitation of carbide will eventually destroy the reversibility of martensite.

2. Damping in Ferrous SMA

The damping measurements carried out in the present study indicate that both ϵ martensite in Fe-Mn-Si-Ni-Cr alloy and α' martensite in Fe-Ni-Ti-Co alloy give rise to high damping. The damping is both strain-amplitude and temperature dependent. The peak loss factor of Fe-Mn-Si-Ni-Cr is 0.04 which falls in between those of NiTi and ferromagnetic alloys. The damping of Fe-Ni-Ti-Co, however, is lower than that of Fe-Mn-Si-Ni-Cr alloy.

The strain-amplitude and temperature dependence, together with the highly nonlinear characteristics of damping suggest that the damping mechanism is related to frictional energy loss associated with the interfacial movement of martensite. This is confirmed by the fact that the temperature of the damping peak of both alloys is in general agreement with the martensitic transformation temperatures. Damping in these ferrous shape memory alloys is thus closely related to their transformation characteristics. With its higher transformation temperature of Fe-Mn-Si-Ni-Cr alloy, the damping peak temperature occurs up to approximately 150°C while that of Fe-Ni-Ti-Co alloy exhibit good damping at subzero transformation temperatures. The damping peak temperature of Fe-Mn-Si-Ni-Cr agrees with the reverse martensitic transformation temperature, which shifts to lower temperatures at higher excitation. This result is consistent with an earlier study concluding that the damping is associated with $\epsilon \rightarrow \gamma$ reverse transformation. The alloy, however, does not exhibit high damping in the fully martensitic state. The behavior seems to be related to the fact that ϵ martensite habit plane variants form intersections with each other. The intersection creates sessile interfaces which prevent the operation of the damping mechanism. The Fe-Ni-Ti-Co alloy, on the other hand, exhibits a good damping plateau at temperatures below the M_s temperature as well as a damping peak at -20°C. The damping plateau is clearly associated with the thermoelastic thin plate martensite. Unlike ϵ martensite, the morphology of thin plate martensite does form as self-accommodation groups and therefore maintains the glissile nature of inter-variant interfaces. The higher temperature damping peak is probably related to pre-existing thin plate martensite as the metallographic study suggests that these martensite plates do thicken on cooling. The result suggests that the martensite/parent interface is somewhat glissile.

Damping in Fe-Mn-Si-Ni-Cr alloys is enhanced by both thermal and mechanical cycling. The effect appears to come from an interaction between the movement of martensite interface and the

defects generated by the transformation and mechanical cycling. The damping in Fe-Ni-Ti-Co alloy increases with aging time at 700°C. The promotion of a thermoelastic transformation raises damping capacity in this case.

The limitation of both the DTMA and the resonance techniques is the excitation strain-amplitude which has a maximum of 10^{-3} . To efficiently utilize the hysteresis energy loss associated with the transformation, the excitation has to be higher than the critical strain to induce either the transformation or the reorientation of the martensite variant. This critical strain is about 0.005, as estimated from Figure 18. The present techniques operate clearly below this critical excitation strain. Nevertheless, present study does demonstrate that both ϵ and α' martensites do give rise to both shape memory effect and good damping.

V. CONCLUSIONS

1. Both ϵ martensite in Fe-Mn-Si-Ni-Cr and α' martensite in Fe-Ni-Ti-Co exhibit high damping with loss factors up to 0.04. The mechanism is associated with the hysteresis energy loss during the movement of martensite interfaces.
2. The damping peak associated with ϵ martensite occurs at the reverse transformation temperature. Lower damping in the fully martensitic state is related to the intersection of habit plane variants which creates sessile interfaces.
3. Higher excitation strain enhances damping of Fe-Mn-Si-Ni-Cr alloy and shifts the damping peak to lower temperatures.
4. Damping in Fe-Ni-Ti-Co alloy appears at temperatures below the M_s temperature. The high damping of martensitic structure comes from the self-accommodation structure which maintains glissile inter-variant interfaces.
5. Increasing damping occurs with aging of Fe-Ni-Ti-Co alloy at 700°C which enhances thermoelasticity of the α' martensite.

REFERENCES

1. L.M. Schetky and J. Perkins, Machine Design, vol. 50, no. 8, pp. 202 (1978).
2. J.A. Hedly, Met. Sci. J., vol. 2, p. 129 (1968).
3. P.R. Witting and F.A. Corrarelli, Shape Memory Structural Dampers: Material Properties, Design and Seismic Testing, National Center for Earthquake Engineering Research, Technical Report NCEER 92-0013, May 1992.
4. L.M. Schetky, M.H. Wu, C.Y. Lei, C. Liang and C. Rogers, Hybrid Composite Materials Using Shape Memory Actuators to Provide Vibration and Acoustic Control, Office of Naval Research, Contract No. N00014-90-C-0164, Final Report (1993).
5. K.P. Roey, A Comparison of CuAlNi and Other High Damping Alloys for the Purpose of Naval Ship Silencing Applications. MS Thesis, Naval Postgraduate School, 1989.
6. K. Enami, S. Nenno and Y. Minato, Scripta Metall., vol. 5, pp. 2343 (1971).
7. A. Sato, E. Chishima and T. Mori, Acta Metall., vol. 30, pp. 1177 (1982).
8. M. Murakami, H. Otsuka, H.G. Suzuki and S. Matsuda, Proceedings, ICOMAT-86, pp. 985 (1986).
9. K. Tsuzaki, Y. Natsume, Y. Kurokawa and T. Maki, Scripta Metall., vol. 27, pp. 471 (1992).
10. NKK Technical Bulletin.
11. H. Otsuka, H. Yamada, H. Takanishi and T. Maruyama, Proceedings, ICOMAT-89 (Materials Science Forum vol. 56-58), pp. 655 (1990).
12. T. Sohmura, R. Oshima and F.E. Fujita, Scripta Metall., vol. 14, pp. 855.
13. R. Oshima, S. Sugimoto, M. Sugiyama, T. Hamada and F.E. Fujita, Trans. JIM, vol. 26, pp. 523 (1985).
14. M. Umemoto and C.M. Wayman, Metall. Trans. A., vol. 9A, pp. 891 (1978).
15. T. Maki, K. Kobayashi, M. Minato and I. Tamura, Scripta Metall., vol. 18, pp. 1177 (1984).
16. T. Maki, S. Shimooka, M. Umetomo and I. Tamura, Trans. JIM, vol. 13, pp. 400 (1972).

17. I. Tamura, Proc. First Jim International Symposium on New Aspect of Martensitic Transformation, Kobe, Japan, p.59 (1976).
18. S. Kajiwara and T. Kikuchi, Phil. Mag., A, vol. 48, p.509 (1983).
19. E. Hornbogen and W.A. Mayer, Z. Metallk., vol. 58, pp. 372 (1967).
20. M. Watanabe and C.M. Wayman, Metall. Trans., vol. 2, pp. 2221 (1971).
21. S. Kajiwara and T. Kikuchi, Acta Metall. Mater., vol. 38, pp. 847 (1990).
22. S. Kajiwara, T. Kikuchi and N. Sakuma, Proceedings, ICOMAT-86, Japan, p. 991 (1986).
23. T. Maki, K. Kobayashi and I. Tamura, Proceedings, ICOMAT-82, Leuven, p.C4-541 (1982).
24. A. Sato, K. Ozaki, Y. Watanabe and T. Mori, Mater. Sci. Eng. A, vol. 101, pp. 25 (1988).
25. A. Sato, Y. Yamaji and T. Mori, Acta Metall., vol. 34, pp. 287 (1986).